



Title	Detection of nuclear spin coherence in GaAs through spin-echo measurements using electrical spin injection
Author(s)	Lin, Zhichao
Citation	北海道大学. 博士(工学) 甲第13517号
Issue Date	2019-03-25
DOI	10.14943/doctoral.k13517
Doc URL	<a href="http://hdl.handle.net/2115/74205">http://hdl.handle.net/2115/74205</a>
Type	theses (doctoral)
File Information	Zhichao_Lin.pdf



[Instructions for use](#)

**Detection of nuclear spin coherence in GaAs  
through spin-echo measurements using  
electrical spin injection**

**Zhichao Lin**

Division of Electronics for Informatics

Graduate School of Information Science and Technology

Hokkaido University

January 2019



# Contents

<b>1. Introduction</b>	<b>1</b>
1.1 Nuclear spins for implementing quantum bits.....	1
1.2 Nuclear spin manipulation using electrical spin injection.....	3
1.3 Nuclear spin coherence time $T_2$ and $T_2^*$ .....	5
1.4 Purpose.....	6
1.5 Overview.....	6
References.....	9
<b>2. Principles of nuclear spin manipulation and electron spin injection</b>	<b>11</b>
2.1 Nuclear spin manipulation.....	11
2.1.1 Nuclear magnetic resonance.....	12
2.1.2 Rabi oscillation.....	13
2.1.3 Spin echo.....	15
2.2 Electron spin injection/detection.....	17
2.2.1 Spin injection/detection using four-terminal non-local geometry.....	17
2.2.2 Spin-valve effect.....	20
2.2.3 Hanle effect.....	22
2.3 Detection of nuclear spins in a spin injection system.....	24
2.3.1 Nuclear field polarized by electron spins.....	24
2.3.2 Detection of NMR from a non-local voltage of electron spins.....	25
References.....	28
<b>3. Electrical spin injection into GaAs-based semiconductors with a highly polarized spin source</b>	<b>31</b>
3.1 Introduction.....	31
3.2 Spin injection into bulk GaAs.....	32
3.2.1 Layer structure and device geometry.....	32
3.2.2 Spin-valve signal and Hanle signal.....	34
3.3 Spin injection into AlGaAs/GaAs heterostructures.....	35
3.3.1 Layer structure and device geometry.....	35

3.3.2 Results and discussion.....	37
3.3.2.1 Mobility and contact resistance.....	37
3.3.2.2 Temperature dependence of spin-valve signal.....	38
3.3.2.3 Spin lifetime.....	42
3.4 Summary and conclusion.....	44
References.....	46
<b>4. Transient analysis of dynamic nuclear polarization</b>	<b>49</b>
4.1 Introduction.....	49
4.2 Simulation model.....	50
4.2.1 Nuclear spin temperature.....	50
4.2.2 Cooling of the nuclear spin system through the DNP process.....	52
4.2.3 Time evolution of the nuclear spin temperature.....	53
4.2.4 Experimental conditions.....	53
4.3 Simulation results and discussion.....	56
4.4 Summary.....	60
References.....	61
<b>5. Detection of nuclear spin coherence through spin-echo measurements</b>	<b>63</b>
5.1 Introduction.....	63
5.2 Experimental methods and results.....	64
5.2.1 Device structure.....	64
5.2.2 Initialization of DNP.....	67
5.2.3 Resonance condition for $^{69}\text{Ga}$ nuclear spins.....	68
5.2.4 Rabi oscillation of $^{69}\text{Ga}$ nuclear spins.....	69
5.2.5 Spin echo signal of $^{69}\text{Ga}$ nuclear spins.....	71
5.3 Discussion.....	74
5.4 Summary.....	75
References.....	76
<b>6. Conclusion</b>	<b>77</b>
<b>Acknowledgements</b>	<b>79</b>
<b>Appendix</b>	<b>81</b>

# 1. Introduction

## 1.1 Nuclear spins for implementing quantum bits

Spintronics is an emerging technology by combining electron charge and spin together to create electronic devices with features of nonvolatility, reconfigurable logic functions, and ultralow power consumption. It is a study of spin phenomena in solids, especially metals and semiconductors. Metal-based spintronic devices such as giant magnetoresistance (GMR) heads and magnetic tunnel junctions (MTJs) have been commercially applied to hard disk drivers (HDDs) as the read heads and magnetic random access memories (MRAMs) as the memory cells, respectively [1, 2]. Although spintronics has achieved a great progress in metal-based devices, the electron spins in semiconductors have not been fully utilized. Compared with the metal-based devices, the main advantage of the semiconductor-based devices is that they can amplify signals, which is indispensable for information processing and communication [3]. Therefore, the development of semiconductor-based spintronic devices is an important step in spintronics.

On the other hand, nuclear spins in semiconductors have attracted much interest for implementing quantum bits (qubits) because they have extremely long coherence times. The nuclear magnetic resonance (NMR) technique enables the control and detection of nuclear-spin-based qubits. However, the sensitivity of the conventional NMR technique is limited by the low magnetic moments of the nuclear spins, which are three orders of magnitude smaller than that of the electron spins. Dynamic nuclear polarization (DNP), where nuclear spins are dynamically polarized through a hyperfine interaction between nuclear spins and electron spins, has attracted much interest, since it can dramatically increase the NMR signal. The hyperfine interaction can be expressed as [4, 5]

$$\mathbf{H} = A\mathbf{I} \cdot \mathbf{S} = A\left[\frac{1}{2}(I_+S_- + I_-S_+) + I_zS_z\right] \quad (1.1)$$

where  $A$  is the hyperfine constant,  $\mathbf{I}$  is the nuclear spin,  $\mathbf{S}$  is the electron spin,  $I_{\pm}$  and  $S_{\pm}$  are the ladder operators of nuclear spins and electron spins, respectively, and  $(I_+S_- + I_-S_+)$  is the spin flip-flop term. In the hyperfine interaction (Fig. 1.1), non-equilibrium polarized electrons transfer their spin angular momentum to the nuclei through spin flip-flop, leading to an effective nuclear spin polarization, referred to as DNP. The polarized nuclear spins will, in turn, affect the electron spins as an effective magnetic field or Overhauser field. Similarly, the polarized electron spins act on the nuclear spins as an effective magnetic field or Knight field [6].

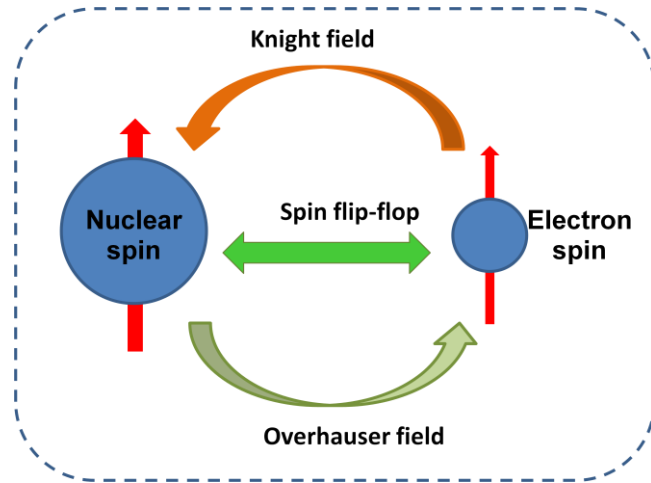


**Fig. 1.1.** Illustration of hyperfine interaction between electron spins and nuclear spins.

To generate electron spins, methods such as optical polarization, quantum Hall system, and electrical spin injection are used. Several instances of DNP in semiconductors induced by optical means or electrical means have been reported [7-22]. Furthermore, coherent manipulation of nuclear spins in semiconductors by NMR with DNP has been demonstrated electrically in GaAs/AlGaAs quantum Hall systems by observing the Rabi oscillation [23-25] and optically in GaAs/AlGaAs quantum wells by observing the Rabi oscillation and spin-echo signals [26]. Although the optical method is suitable for clarifying the fundamental physics of nuclear spins, it is restricted in its scalability because the spatial resolution is limited by the optical wavelength. The quantum Hall systems require a strong magnetic field of several Tesla and a low temperature below 1 K to create highly polarized electron

spins for DNP. Considering these shortcomings, a spin injection system is a better choice since it is all electrical and a highly polarized spin source allows efficient DNP without a strong magnetic field.

## 1.2 Nuclear spin manipulation using electrical spin injection

Recently, we developed an NMR system that uses spin injection from a highly polarized spin source and detected the Rabi oscillation electrically with a static magnetic field of  $\sim 0.1$  T at 4.2 K [27]. Figure 1.2 shows the device structure of the NMR system. The device operation includes:

1) Generation of electron spin polarization in semiconductor by spin injection.

A half-metallic ferromagnet of  $\text{Co}_2\text{MnSi}$  is used as a spin source for an efficient spin injection into GaAs because it provides 100% electron spin polarization at the Fermi level. By applying a bias current between electrode-2 and electrode-1, electron spins are injected from  $\text{Co}_2\text{MnSi}$  into GaAs.

2) Initialization of nuclear spins by DNP.

The nuclear spins are dynamically polarized by electron spins, resulting in an increased nuclear spin polarization.

3) Quantum manipulation of nuclear spins through NMR effect.

NMR effect is used to control the nuclear spins and the changes of the nuclear spin states result in changes in the nuclear field.

4) Readout of nuclear spin states through the detection of the non-local voltage ( $V_{\text{NL}}$ ) between electrode-3 and electrode-4.

The non-local voltage is a measure of the response of the electron spins to the effective magnetic field including a static magnetic field and a nuclear field. Since the nuclear spins affect the electron spins as a nuclear field, any change in the nuclear spin state will lead to a change in the nuclear field, resulting in a change in  $V_{\text{NL}}$ .

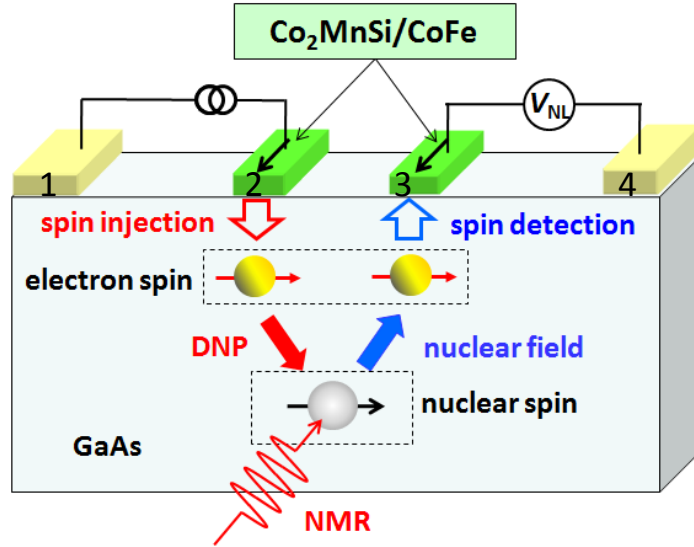


**Fig. 1.2.** Device structure of an NMR system using electrical spin injection.

Figure 1.3 shows an illustration of Rabi oscillation. An rf magnetic field  $\mathbf{B}_{\text{rf}}$  applied to the nuclear spin system induces nuclear spin transition between two-level states. The transition of the nuclear spins leads to an oscillation behavior in the  $z$  component of the nuclear spins, which is known as Rabi oscillation. One important thing is that the coherence time  $T_2^*$  of the nuclear spins can be estimated from the decay time  $T_2^{\text{Rabi}}$  of the Rabi oscillation as  $T_2^* = 1/2T_2^{\text{Rabi}}$  [28]. The coherence time  $T_2^*$  consists of an intrinsic component  $T_2$ , which results from the dipolar-dipolar interaction between the nuclear spins, and the other component  $T_2^{\text{inhom}}$ , which results from the inhomogeneity in the external magnetic field. The main purpose of this study is to estimate the intrinsic coherence time  $T_2$  of the nuclear spins.

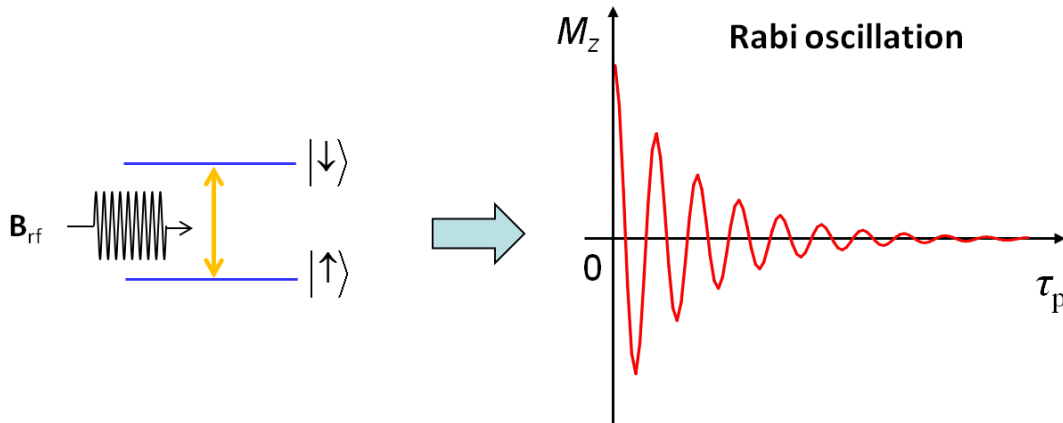


**Fig. 1.3.** Illustration of Rabi oscillation.

### 1.3 Nuclear spin coherence time $T_2$ and $T_2^*$

A nuclear spin system can be characterized by two different relaxation times,  $T_1$  and  $T_2$ .  $T_1$  describes the longitudinal relaxation of the nuclear spin magnetization, while  $T_2$  describes the transverse relaxation.  $T_1$  is far greater than  $T_2$  in most cases and it is not related to this study.  $T_2$  is the coherence time related to the qubits. Figure 1.4 shows the illustration of the decoherence of the nuclear spins. Besides the external magnetic field  $\mathbf{B}_{\text{ext}}$ , the nuclear spins can see a local field  $\mathbf{B}_L$  generated by the neighbor nuclear spins. The nuclear spins rotate along the effective magnetic field  $\mathbf{B} = \mathbf{B}_{\text{ext}} + \mathbf{B}_L$  with a frequency  $\omega = -\gamma|\mathbf{B}|$ , where  $\gamma$  is the gyromagnetic ratio [29]. If the nuclear spins rotate with an identical frequency, then the coherence is remained. Since the local field is random, the effective magnetic field experienced by each nuclear spin is different and they rotate with a different frequency, and therefore the phase for each nuclear spin becomes different, resulting in the decoherence with a time scale of  $T_2$ . For achieving nuclear-spin-based qubits, it is important to clarify the nuclear-spin phase coherence time  $T_2$ , because the lifetime of a qubit is limited by  $T_2$ . In a real system, however, the decoherence is enhanced due to the inhomogeneity in the external magnetic field. The real coherence time is known as  $T_2^*$ , and it consists of an intrinsic component  $T_2 = 1/\gamma B_L$ , which results from the dipolar-dipolar interaction between the nuclear spins, and the other component  $T_2^{\text{inhom}} = 1/\gamma \Delta B_{\text{ext}}$ , which results from the inhomogeneity in the external magnetic field.  $T_2$  is the intrinsic coherence time and it is determined by the material itself while  $T_2^{\text{inhom}}$  is extrinsic and determined by the measurement system. In order to know the intrinsic  $T_2$ , a spin echo measurement [26, 30], which refocuses nuclear-spin magnetization by using a specific pulse sequence, has to be made to exclude the  $T_2^{\text{inhom}}$  component.

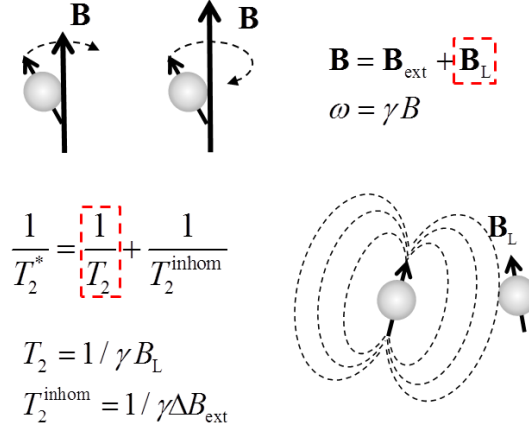


**Fig. 1.4.** Illustration of decoherence of nuclear spins with  $T_2$  and  $T_2^*$ .

## 1.4 Purpose

The purpose of this study is to clarify the intrinsic coherence time of the nuclear spins in GaAs through an electrical spin-echo measurement in a spin injection device. The broad purpose is to develop a spin-injection combined NMR technique for nuclear-spin manipulation. Specifically, electrical spin injection into GaAs-based semiconductors with a highly polarized spin source is investigated at first. Then the DNP process in GaAs is investigated and analyzed for a better understanding of nuclear spin physics. Last but most importantly, an NMR-based nuclear spin manipulation system using spin injection is developed and the nuclear spin coherence time is investigated in GaAs.

## 1.5 Overview

This dissertation is organized as follows:

Chapter 1 introduces the background and the purpose of this study. Nuclear spins in semiconductors are an ideal system for implementing quantum bits because of their extremely long coherence time. Recently, we developed an NMR system that uses spin injection from a highly polarized spin source to effectively polarize the

nuclear spins and demonstrated coherent manipulation of nuclear spins. However, the intrinsic coherence time of the nuclear spins has not been investigated yet. The purpose of this study is to clarify the intrinsic coherence time of the nuclear spins in GaAs through an electrical spin-echo measurement in a spin injection device.

Chapter 2 covers the theoretical principles of NMR, Rabi oscillation, spin echo, as well as electron spin injection/detection.

Chapter 3 describes the results of spin injection into bulk GaAs [31] and AlGaAs/GaAs heterostructures [32] with a highly polarized spin source. In bulk GaAs, a clear spin-valve signal and a Hanle signal were observed. The highly polarized spin source of  $\text{Co}_2\text{MnSi}$  resulted in a high spin polarization, which is promising for the DNP process. Moreover, a clear transient oblique Hanle signal was observed, which was evidence of nuclear spin polarization. In the AlGaAs/GaAs heterostructure, a spin-valve signal was observed up to room temperature. The temperature dependence of the spin-valve signal shows relatively complicated behavior compared with that of the bulk device, which results from the opposite tendency of sheet resistance. Moreover, the spin-valve signal in the AlGaAs/GaAs heterostructure is less sensitive to temperature than that in bulk GaAs. This result contributes to a better understanding of spin transport in a two-dimensional channel, which is indispensable for realizing future spin transistors that can operate at room temperature.

Chapter 4 analyzes the transient behavior of nuclear spins in the presence of DNP using the concept of nuclear spin temperature [33] for a better understanding of nuclear spin dynamics.

Chapter 5 describes the detection of nuclear spin coherence time in GaAs through a spin-echo measurement [31]. All the measurements were done at a low magnetic field of approximately 0.1 T and a relatively high temperature of 4.2 K because the highly polarized  $\text{Co}_2\text{MnSi}$  spin source enabled efficient DNP. First, Rabi oscillation, which is an oscillation behavior of nuclear spins along an rf-magnetic field, was measured to determine the pulse durations for the spin-echo measurement. Then the spin-echo measurement was conducted. It was found that the intrinsic

coherence time  $T_2$  obtained from the spin-echo signals was slightly larger than  $T_2^*$  obtained by the Rabi oscillation, which indicates that the inhomogeneity in the external fields exists. In our device, the external fields consist of a static field, a stray field from the ferromagnet, and an electron field generated by the electron spins. Since the device has nanoscale dimensions, the inhomogeneity in the static field is probably negligible. Therefore, the inhomogeneity probably comes from the stray field or the electron field.

Finally, chapter 6 summarizes the results and makes a conclusion.

## References

- [1] S. A. Wolf, D. D. Awschalom, R. A. Buhrman, J. M. Daughton, S. von Molnár, M. L. Roukes, A. Y. Chtchelkanova and D. M. Treger, *Science* **294**, 1488 (2001).
- [2] I. Žutić, J. Fabian, and S. Das Sarmar, *Rev. Mod. Phys.* **76**, 323 (2004).
- [3] D. D. Awschalom and M. E. Flatté, *Nat. Phys.* **3**, 153 (2007).
- [4] M. I. Dyakonov, in *Spin Physics in Semiconductors*, ed. M. I. Dyakonov (Springer, Heidelberg, 2008), Chap. 1.
- [5] C. Kittel, in *Introduction to Solid State Physics*, ed. C. Kittel (Chemical Industry Press, Beijing, 2005), Chap. 13.
- [6] M. I. Dyakonov, in *Spin Physics in Semiconductors*, ed. M. I. Dyakonov (Springer, Heidelberg, 2008), Chap. 11.
- [7] M. I. Dyakonov, V. I. Perel, V. L. Berkovits, and V. I. Safarov, *Sov. Phys. JETP* **40**, 950 (1975).
- [8] D. Paget, G. Lampel, B. Sapoval, and V. I. Safarov, *Phys. Rev. B* **15**, 5780 (1977).
- [9] G. Lampel, *Phys. Rev. Lett.* **20**, 491 (1968).
- [10] J. Strand, B. D. Schultz, A. F. Isakovic, C. J. Palmstrøm, and P. A. Crowell, *Phys. Rev. Lett.* **91**, 036602 (2003).
- [11] D. Gammon, S. W. Brown, E. S. Snow, T. A. Kennedy, D. S. Katzer, and D. Park, *Science* **277**, 85 (1997).
- [12] G. Salis, D. T. Fuchs, J. M. Kikkawa, and D. D. Awschalom, *Phys. Rev. Lett.* **86**, 2677 (2001).
- [13] T. Machida, T. Yamazaki, and S. Komiyama, *Appl. Phys. Lett.* **80** 4178 (2002).
- [14] K. Hashimoto, K. Muraki, T. Saku, and Y. Hirayama, *Phys. Rev. Lett.* **88**, 176601 (2002).
- [15] M. Poggio, G.M. Steeves, R. C. Myers, Y. Kato, A. C. Gossard, and D. D. Awschalom, *Phys. Rev. Lett.* **91**, 207602 (2003).
- [16] K. Ono and S. Tarucha, *Phys. Rev. Lett.* **92**, 256803 (2004).
- [17] J. Strand, X. Lou, C. Adelman, B. D. Schultz, A. F. Isakovic, C. J. Palmstrøm, and P. A. Crowell, *Phys. Rev. B* **72**, 155308 (2005).

- [18] P. Van Dorpe, W. Van Roy, J. De Boeck, and G. Borghs, Phys. Rev. B **72**, 035315 (2005).
- [19] M. K. Chan, Q. O. Hu, J. Zhang, T. Kondo, C. J. Palmstrøm, and P. A. Crowell, Phys. Rev. B **80**, 161206(R) (2009).
- [20] G. Salis, A. Fuhrer, and S. F. Alvarado, Phys. Rev. B **80**, 115332(R) (2009).
- [21] J. Shiogai, M. Ciorga, M. Utz, D. Schuh, T. Arakawa, M. Kohda, K. Kobayashi, T. Ono, W. Wegscheider, D. Weiss, and J. Nitta, Appl. Phys. Lett. **101**, 212402 (2012).
- [22] T. Akiho, J. Shan, H. -x. Liu, K. -i. Matsuda, M. Yamamoto, and T. Uemura, Phys. Rev. B. **87**, 235205 (2013).
- [23] T. Machida, T. Yamazaki, K. Ikushima, and S. Komiyama, Appl. Phys. Lett. **82**, 409 (2003).
- [24] G. Yusa, K. Muraki, K. Takashina, K. Hashimoto, and Y. Hirayama, Nature (London) **434**, 1001 (2005).
- [25] H. Takahashi, M. Kawamura, S. Masubuchi, K. Hamaya, T. Machida, Y. Hashimoto, and S. Katsumoto, Appl. Phys. Lett. **91**, 092120 (2007).
- [26] H. Sanada, Y. Kondo, S. Matsuzaka, K. Morita, C.Y. Hu, Y. Ohno, and H. Ohno, Phys. Rev. Lett. **96**, 067602 (2006).
- [27] T. Uemura, T. Akiho, Y. Ebina, and M. Yamamoto, Phys. Rev. B **91**, 140410(R) (2015).
- [28] H. C. Torrey, Phys. Rev. **76**, 1059 (1949).
- [29] C. Kittel, *Introduction to Solid State Physics* (John Wiley & Sons, Inc, USA, 1996).
- [30] A. Abragam, *The Principles of Nuclear Magnetism* (Clarendon, Oxford, 1961).
- [31] Z. Lin, M. Rasly, and T. Uemura, Appl. Phys. Lett. **110**, 232404 (2017).
- [32] Z. Lin, D. Pan. M. Rasly, and T. Uemura, Appl. Phys. Lett. (in press).
- [33] Z. Lin, K. Kondo, M. Yamamoto, and T. Uemura, Jpn. J. Appl. Phys. **55**, 04EN03 (2016).

## 2. Principles of nuclear spin manipulation and electron spin injection

### 2.1 Nuclear spin manipulation

Nuclear magnetic resonance (NMR) offers a method for nuclear spin manipulation, and it has been widely used in chemical analysis and bioimaging. In this section, the principle of NMR will be introduced (Fig. 2.1). Rabi oscillation is an oscillation behavior of the  $z$  component of the nuclear spin magnetization due to the nuclear spin transition between two-level states. Spin echo is the refocusing of the nuclear spins by a pulse sequence. Both Rabi oscillation and spin echo are based on pulse NMR. Rabi oscillation should be measured ahead to determine the pulse length for the spin-echo measurement. Then a spin-echo measurement can be conducted to determine  $T_2$ .

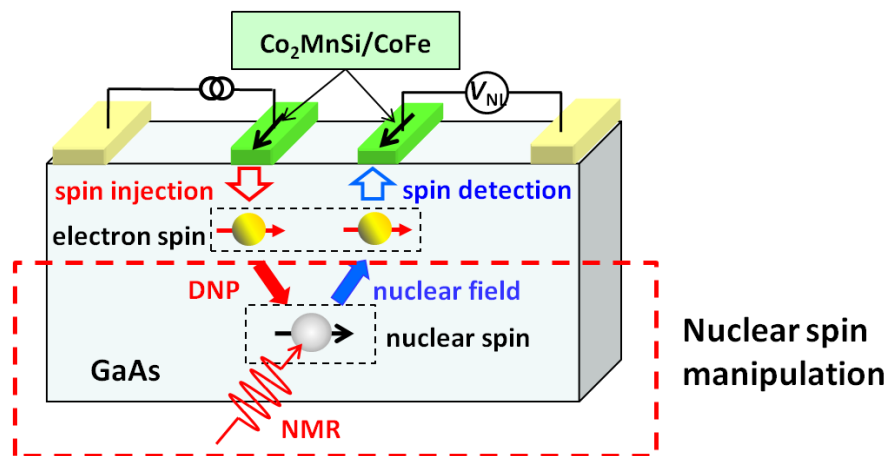


Fig. 2.1. Illustration of nuclear spin manipulation in a spin injection system

## 2.1.1 Nuclear magnetic resonance

The NMR technique enables the control and detection of nuclear spins. In the presence of a static magnetic field  $\mathbf{B}_0$ , the nuclear spins split as up spin and down spin with different energy levels, and the energy gap between down spin and up spin is given by [1]

$$\Delta E = \hbar \gamma |\mathbf{B}_0|, \quad (2.1)$$

where  $\hbar$  is the reduced Planck constant, and  $\gamma$  is the gyromagnetic ratio of the nuclear spins. When an irradiated rf-magnetic field  $\mathbf{B}_{\text{rf}}$  with the same energy of  $\Delta E$  is applied to the nuclear spin system, the nuclear spins will absorb energy from  $\mathbf{B}_{\text{rf}}$  or re-emit energy as photons, leading to the transition of nuclear spins between two-level states (Fig. 2.2(a)). The resonance condition is given by [1]

$$2\pi f_{\text{rf}} = \gamma |\mathbf{B}_0|, \quad (2.2)$$

where  $f_{\text{rf}}$  is the frequency of  $\mathbf{B}_{\text{rf}}$ .

Considering the nuclear spins in a coordinate axis with a static magnetic field  $\mathbf{B}_0$  along the  $z$ -axis, the nuclear spins will precess along  $\mathbf{B}_0$  with a frequency  $\omega = -\gamma |\mathbf{B}_0|$  (Fig. 2.2(b)). The rf-magnetic field  $\mathbf{B}_{\text{rf}}$  should be applied perpendicular to  $\mathbf{B}_0$  along the  $x$ -axis.  $\mathbf{B}_{\text{rf}}$  can be decomposed as

$$\begin{aligned} \mathbf{B}_{\text{rf}}(t) &= |\mathbf{B}_{\text{rf}(m)}| \cos(\omega t) \mathbf{a}_x \\ &= \frac{1}{2} |\mathbf{B}_{\text{rf}(m)}| \{ \cos(\omega t) \mathbf{a}_x + \sin(\omega t) \mathbf{a}_y \} + \frac{1}{2} |\mathbf{B}_{\text{rf}(m)}| \{ \cos(-\omega t) \mathbf{a}_x + \sin(-\omega t) \mathbf{a}_y \}, \end{aligned} \quad (2.3)$$

where  $\mathbf{B}_{\text{rf}(m)}$  is the amplitude of  $\mathbf{B}_{\text{rf}}$ , and  $\omega = \gamma |\mathbf{B}_0|$  is the angular velocity of  $\mathbf{B}_{\text{rf}}$ . From this equation, we can see  $\mathbf{B}_{\text{rf}}$  can be treated as a sum of two rotating components (Fig. 2.2(b)). Both components rotate in the  $xy$ -plane, at the same frequency, but in opposite directions. The component, which has the same rotation direction with the nuclear spins is static to the nuclear spins, and consequently contributes to the resonance by rotating the nuclear spins.

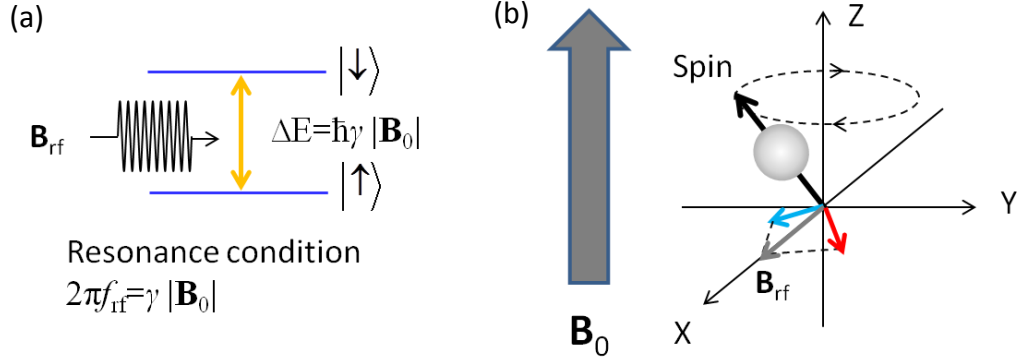


**Fig. 2.2.** Illustration of NMR by a) nuclear spin transition between two-level states, b) rotation of the nuclear spins by the resonance component of  $\mathbf{B}_{\text{rf}}$ .

### 2.1.2 Rabi oscillation

Considering the nuclear spins in a rotating axis which rotates along the  $z$ -axis with a rotating frequency synchronized to the resonance frequency of the nuclear spins under a static magnetic field  $\mathbf{B}_0$  (Fig. 2.3), the net spin at equilibrium is parallel to  $\mathbf{B}_0$  along the  $z$ -axis. If an rf-magnetic field  $\mathbf{B}_{\text{rf}}$  with a resonance frequency is applied to the nuclear spins along the  $x$ -axis, the net spin will rotate along  $\mathbf{B}_{\text{rf}}$  with an angle  $\theta = \gamma|\mathbf{B}_{\text{rf}(m)}|\tau_p/2$ , where  $\tau_p$  is the pulse duration of  $\mathbf{B}_{\text{rf}}$ . By plotting the  $\tau_p$  dependence of the  $z$  component of the nuclear spin magnetization, the Rabi oscillation is obtained (Fig. 2.3) and the  $z$  component of the nuclear spin magnetization can be expressed as

$$M_z(\tau_p) = M_0 \cos(2\pi f_{\text{Rabi}} \tau_p) \exp(-\tau_p / T_2^{\text{Rabi}}), \quad (2.4)$$

where  $M_0$  is the equilibrium value of the nuclear spins,  $f_{\text{Rabi}} = \gamma|\mathbf{B}_{\text{rf}(m)}|/4\pi$  is the frequency of the Rabi oscillation where  $\gamma$  is the gyromagnetic ratio of the nuclear spins, and  $T_2^{\text{Rabi}}$  is the decay time of the Rabi oscillation.

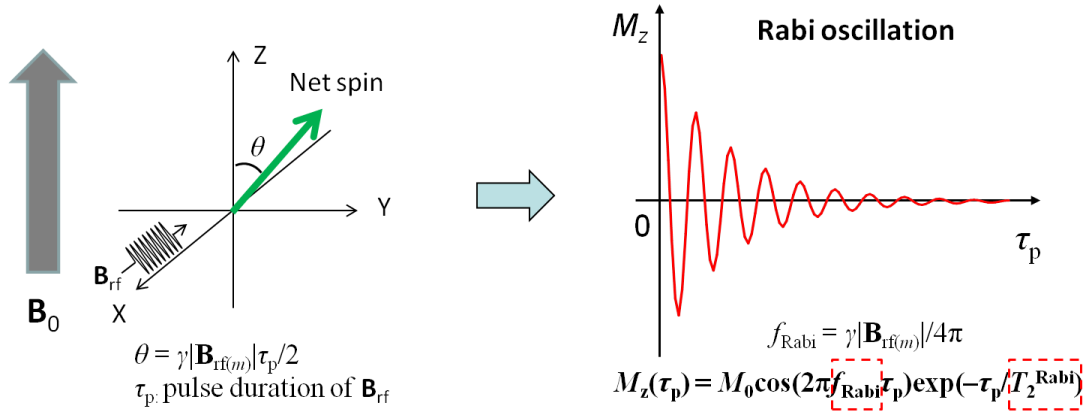


**Fig. 2.3.** Illustration of Rabi oscillation.

One important thing is that the coherence time  $T_2^*$  of the nuclear spins can be estimated as  $T_2^* = 1/2T_2^{\text{Rabi}}$  [2]. The coherence time  $T_2^*$  consists of an intrinsic component  $T_2$ , which results from the dipolar-dipolar interaction between the nuclear spins, and the other component  $T_2^{\text{inhom}}$ , which results from the inhomogeneity in the external magnetic field. To exclude the inhomogeneous component, a spin-echo measurement has to be conducted.

To conduct a spin-echo measurement, a pulse sequence consisting of  $\pi/2$  pulse,  $\pi$  pulse, and  $\pi/2$  pulse is necessary. A  $\pi/2$  pulse rotates the nuclear spin by an angle  $\theta = \pi/2$  and a  $\pi$  pulse rotates the nuclear spin by an angle  $\theta = \pi$ . To determine the durations for the  $\pi/2$  and  $\pi$  pulses, the Rabi oscillation of the nuclear spins should be measured ahead, and the pulse durations  $\tau_p(\theta = \pi/2)$  and  $\tau_p(\theta = \pi)$  can be read from the Rabi oscillation as shown in Fig. 2.4.

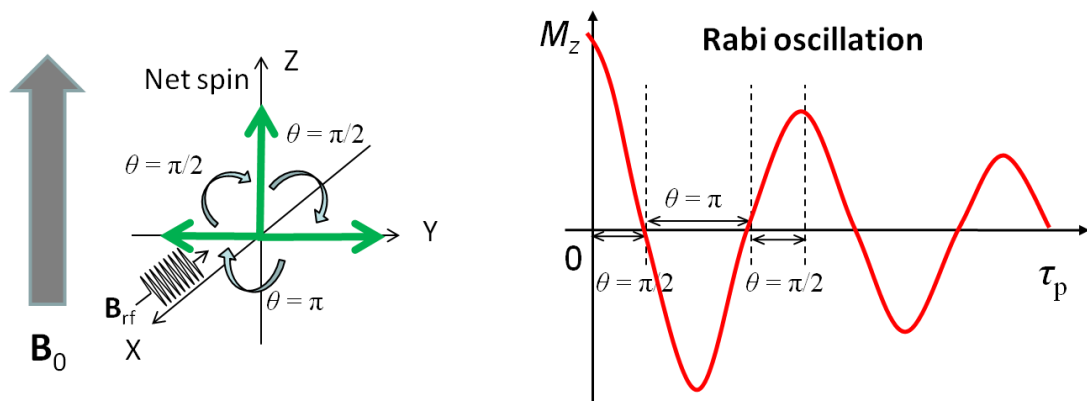


**Fig. 2.4.** Illustration of Rabi oscillation to determine the pulse durations for  $\pi/2$  and  $\pi$  pulses.

### 2.1.3 Spin echo

In the spin echo measurement, a pulse sequence consisting of  $\pi/2$ ,  $\pi$ , and  $\pi/2$  pulses (Fig. 2.5) is applied to nuclear spins that are initialized to be along the  $z$ -axis (Fig. 2.5(a)). The first  $\pi/2$  pulse rotates the nuclear spins by  $\theta = \pi/2$  to the  $y$ -axis in the rotating frame (Fig. 2.5(b)), and the nuclear spins start to dephase due to the inhomogeneous external magnetic field. After a time of  $\tau/2$ , the nuclear spins split because each nuclear spin rotates with a different speed (Fig. 2.5(c)). Some nuclear spin rotates fast and the rotation angle from the  $y$ -axis is larger, and some nuclear spin rotates slowly and the rotation angle from the  $y$ -axis is smaller. At this time, if we apply a  $\pi$  pulse, then the nuclear spins are rotated along the  $x$ -axis by  $\theta = \pi/2$  and they start to refocus (Fig. 2.5(d)), which is just the reversal process of the dephasing in Fig. 2.5(c). After the same time of  $\tau/2$ , the nuclear spins will rotate to the minus  $y$ -axis with an angle equal to that they just rotated from the  $y$ -axis. Then a complete refocusing, or spin echo, occurs (Fig. 2.5(e)). The refocusing can occur because the dephasing due to the inhomogeneous external magnetic field is reversible. Finally, the second  $\pi/2$  pulse rotates the nuclear spins back to the  $z$ -axis for readout (Fig. 2.5(f)). After the application of the pulse, the nuclear field decays due to the local field  $\mathbf{B}_L$ , resulting in a change in the effective magnetic field, which can be detected by the non-local voltage  $V_{NL}$ .

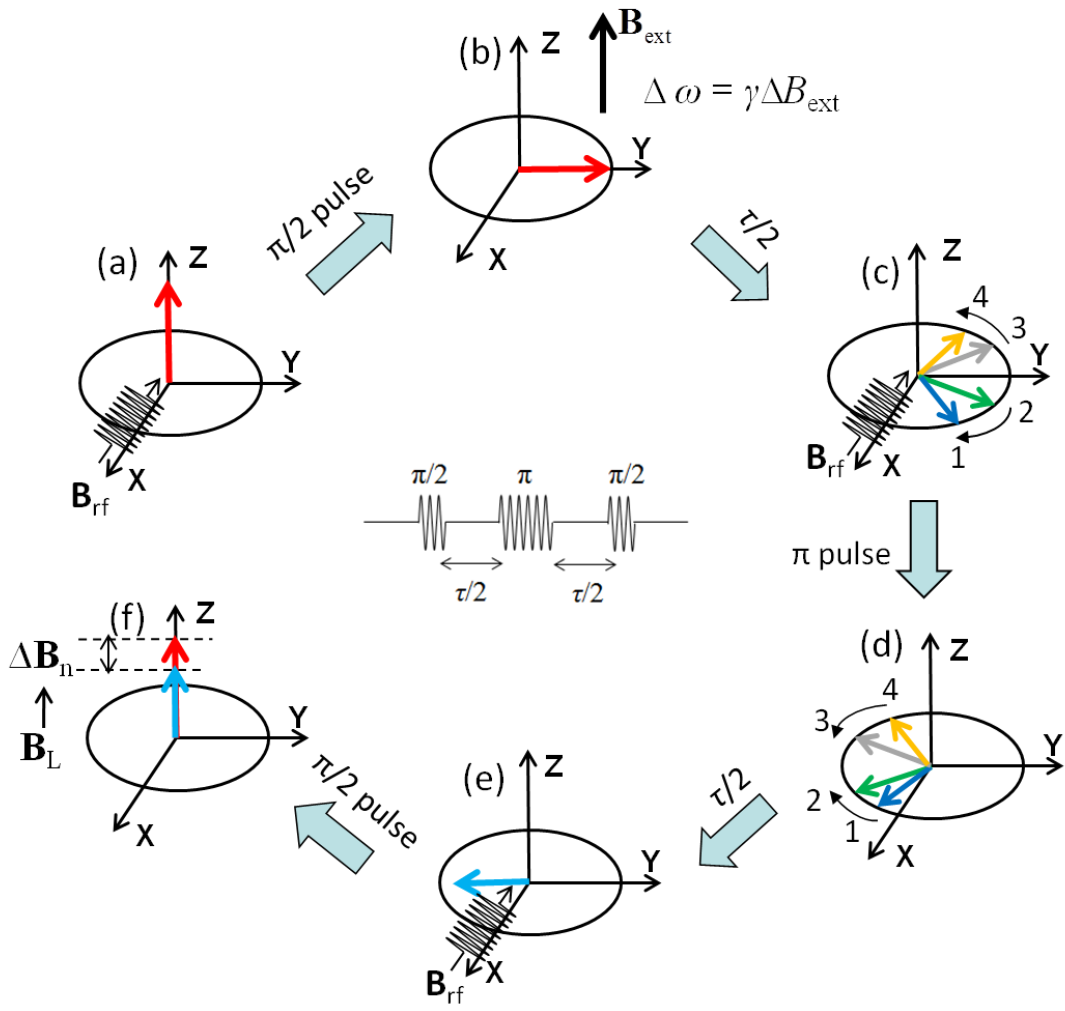


**Fig. 2.5.** Illustration of a spin-echo measurement in a rotating frame with a pulse sequence consisting of  $\pi/2$ ,  $\pi$ , and  $\pi/2$  pulses. The effective RF magnetic field is along the x-axis.

## 2.2 Electron spin injection/detection

In this section, the principle of electron spin injection and detection will be introduced. A four-terminal non-local geometry (Fig. 2.6) is used for spin injection/detection, and spin-valve effect and Hanle effect are used to demonstrate successful spin injection.

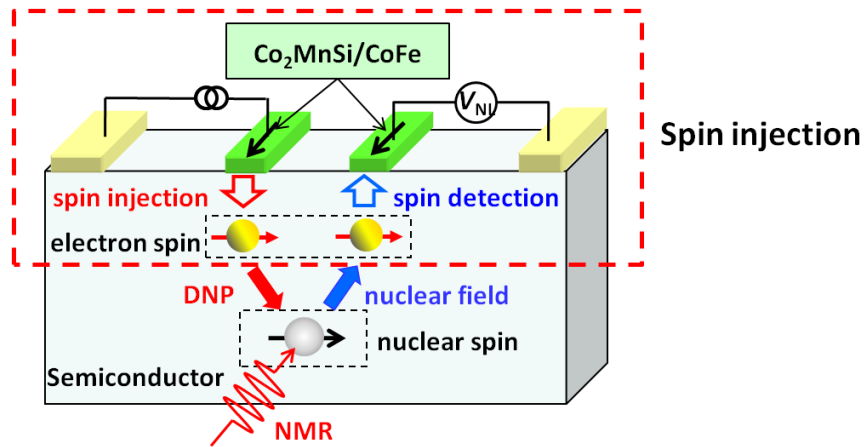
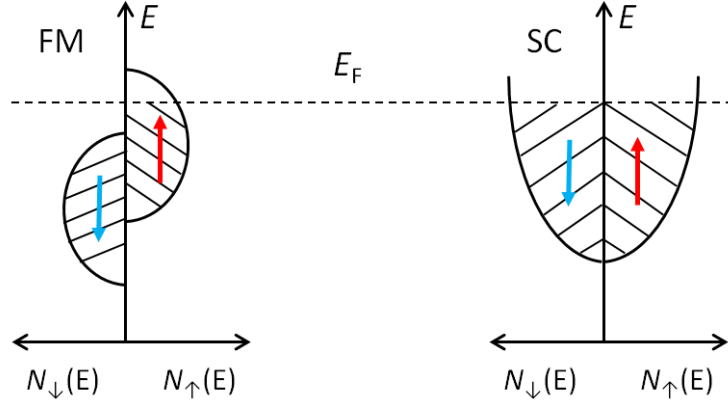


Fig. 2.6. Illustration of electron spin injection/detection.

### 2.2.1 Spin injection/detection using four-terminal non-local geometry

The electron spins have two spin states, and it is conventional to refer to the majority spin as “up spin” while the minority spin is “down spin”. Since the densities of states (DOS) of two spin states are equal in semiconductors (Fig. 2.7) at the Fermi level, the spin polarization is zero. In contrast, the DOS of two spin states are different in ferromagnetic materials. The spin asymmetry in the density of states in ferromagnets allows nonequilibrium spin injection into semiconductors.



**Fig. 2.7.** Density of states of electron spins of ferromagnets (FM) and semiconductors (SC).

To demonstrate spin injection/detection in semiconductors, a four-terminal non-local geometry (Fig. 2.8(a)) is widely used [3-5]. In Fig. 2.8(a), four electrodes are formed on top of a semiconductor channel, among which electrode 2 and 3 are ferromagnets and electrode 1 and 4 are nonmagnetic metals. By applying a constant current between electrode 1 and 2, electron spins are injected from electrode 2 (FM2) into the semiconductor. The injected electron spins will drift towards electrode 1 due to the electric force. In addition, the electron spins will diffuse in the semiconductor due to the inhomogeneity in spin densities. The electron spins diffuse to the right side of electrode 2 and can be detected by electrode 3 (FM3) as a voltage  $V_{NL}$  between electrode 3 and 4. The density of state diagrams for spin injection and detection are shown in Fig. 2.8(b). Because the spin detector (FM3) is placed outside the path of the current, the measured voltage  $V_{NL}$  is called non-local voltage. The four-terminal non-local geometry is used to minimize the background effects, such as the magnetoresistance in the electrodes, local Hall effects, and other extrinsic contributions to the signal.

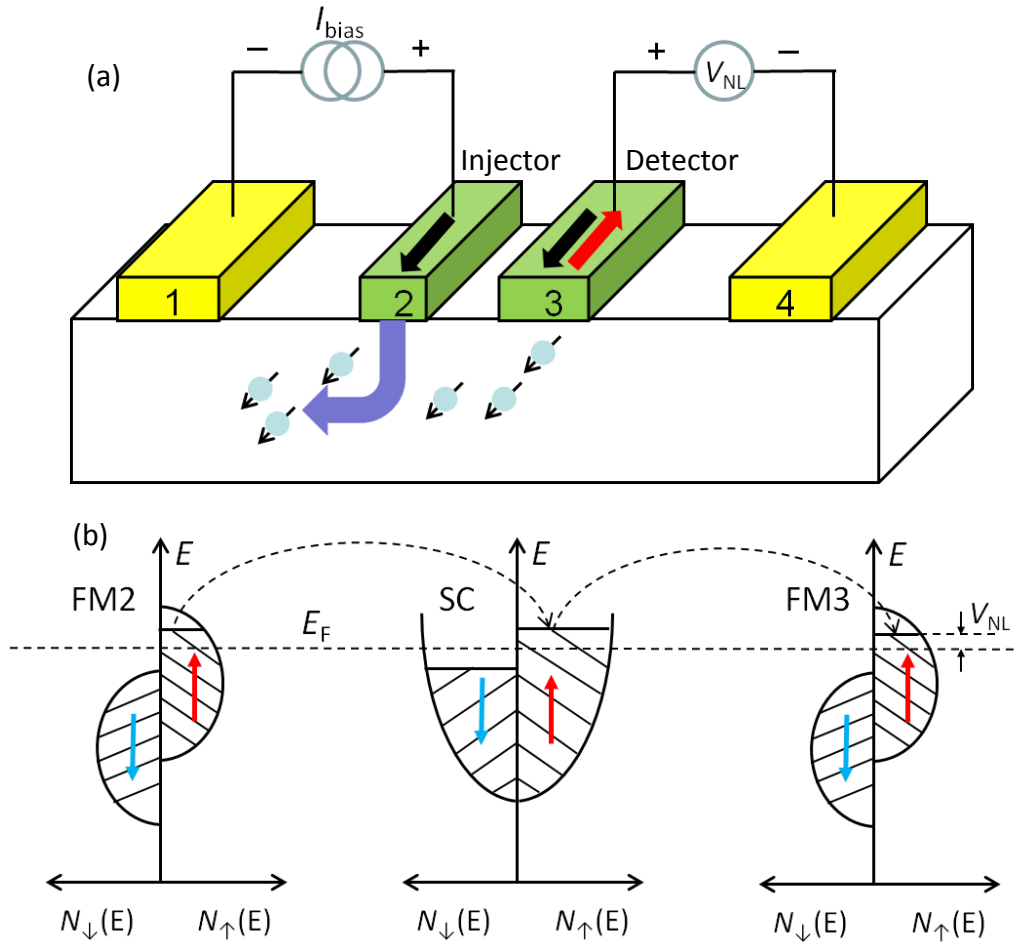


**Fig. 2.8.** (a) Four-terminal non-local geometry and circuit configuration for spin injection/detection. (b) Density of state diagrams for spin injection from FM2 into SC and spin detection at FM3.

### 2.2.2 Spin-valve effect

In the spin-valve measurements, an in-plane magnetic field is swept to change the magnetization configuration between injector (FM2) and detector (FM3) and the magnetization configuration dependence of the non-local voltage is measured (Fig. 2.9). The non-local voltage with parallel (P) or anti-parallel (AP) configuration is given by [6]

$$V_{\text{NL}}^{\text{P(AP)}} = \pm \frac{1}{2} P_{\text{det}} P_{\text{inj}} I_{\text{bias}} \left( \rho \frac{l_{\text{sf}}}{S} \right) \exp\left( -\frac{d}{l_{\text{sf}}} \right), \quad (2.5)$$

where  $P_{\text{inj}}$  and  $P_{\text{det}}$  are the spin polarizations of injector and detector, respectively,  $I_{\text{bias}}$  is the spin injection current,  $\rho$  is the channel resistivity,  $S$  is the cross section of the channel,  $l_{\text{sf}}$  is the spin diffusion length, and  $d$  is the distance between the injector and the detector.

To avoid the tunneling anisotropic magnetoresistance effect (TAMR) in the non-local voltage [7], the in-plane magnetic field should be applied in the easy axis of the electrodes. In the device shown in Fig. 2.9(a), the easy axes for both injector and detector are along the  $y$ -axis. Since there is a difference in the chemical potential between up spin and down spin under the detector (Fig. 2.9(b)), the spin can be detected as a non-local voltage. When the injector and detector are in parallel configuration, majority spins are detected by the detector. By sweeping the in-plane magnetic field, the configuration between the injector and detector switches to the anti-parallel case, in which minority spins are detected. This magnetization configuration switch results in the change in the non-local voltage as shown in Fig. 2.9(c).

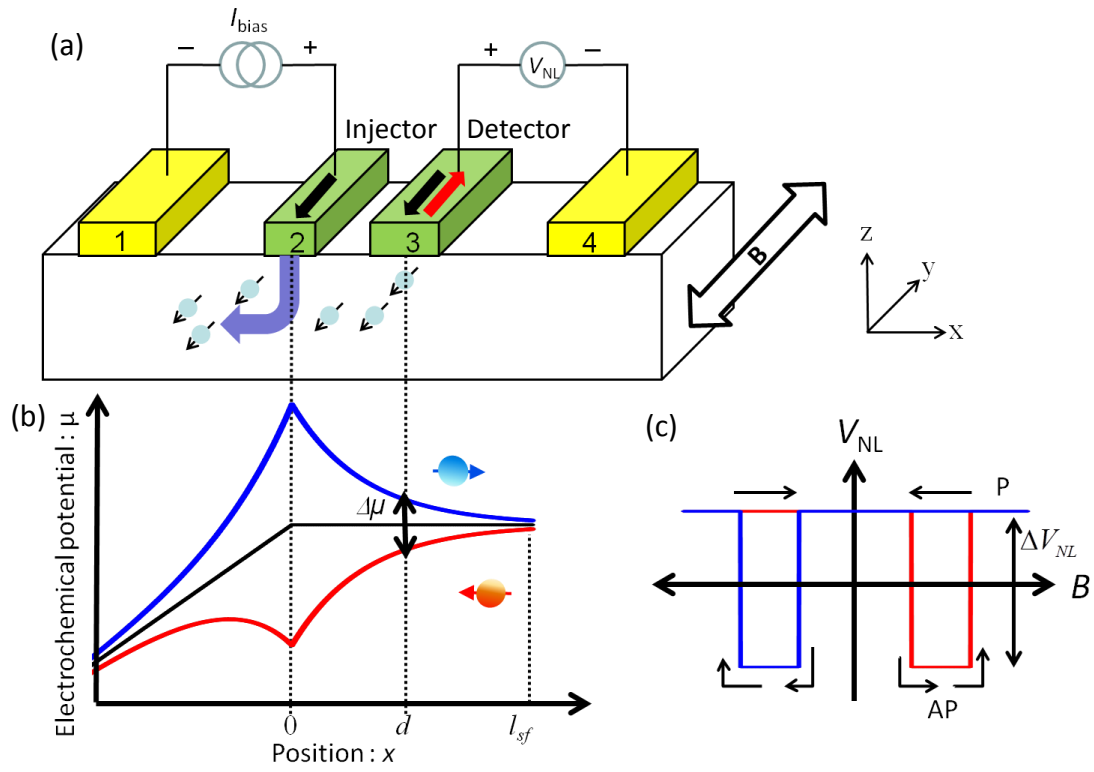


**Fig. 2.9.** Illustration of the spin-valve effect including a) device structure and circuit configuration, b) electrochemical potential for up spin and down spin, and c) an example of a spin-valve signal.

### 2.2.3 Hanle effect

In the Hanle effect measurement, a perpendicular magnetic field is applied to the spin injection device (Fig. 2.10(a)). The electron spins precess and dephase along the magnetic field, resulting in a decrease in the chemical potential difference between up spin and down spin (Fig. 2.10(b)). Consequently, the non-local voltage decays. The non-local voltage with parallel (P) or anti-parallel (AP) configuration is given by [8, 9]

$$V_{\text{NL}}(B_z) = \pm P_{\text{inj}} P_{\text{det}} \left( \frac{\rho l_{\text{sf}}}{S} \right) \left( \frac{l_{\text{sf}}}{\tau_s} \right) I_{\text{bias}} \int_0^{\infty} \frac{1}{\sqrt{4Dt}} \exp\left(-\frac{d^2}{4Dt}\right) \cos(\omega_L t) \exp\left(-\frac{t}{\tau_s}\right) dt, \quad (2.6)$$

where  $\tau_s$  is the spin lifetime,  $D = l_{\text{sf}}^2 / \tau_s$  is the diffusion constant,  $\omega_L = g\mu_B B_z / \hbar$  is the Larmor frequency, where  $g$  is the electron  $g$  factor,  $\mu_B$  is the Bohr magneton, and  $\hbar$  is the reduced Planck's constant.

In the parallel (anti-parallel) configuration, majority (minority) spins are detected. Due to the precession and dephasing of the electron spins along the magnetic field, the number of majority (minority) spins decreases (increases) as the magnetic field increases, resulting in the change in the non-local voltage as shown in Fig. 2.10(c).

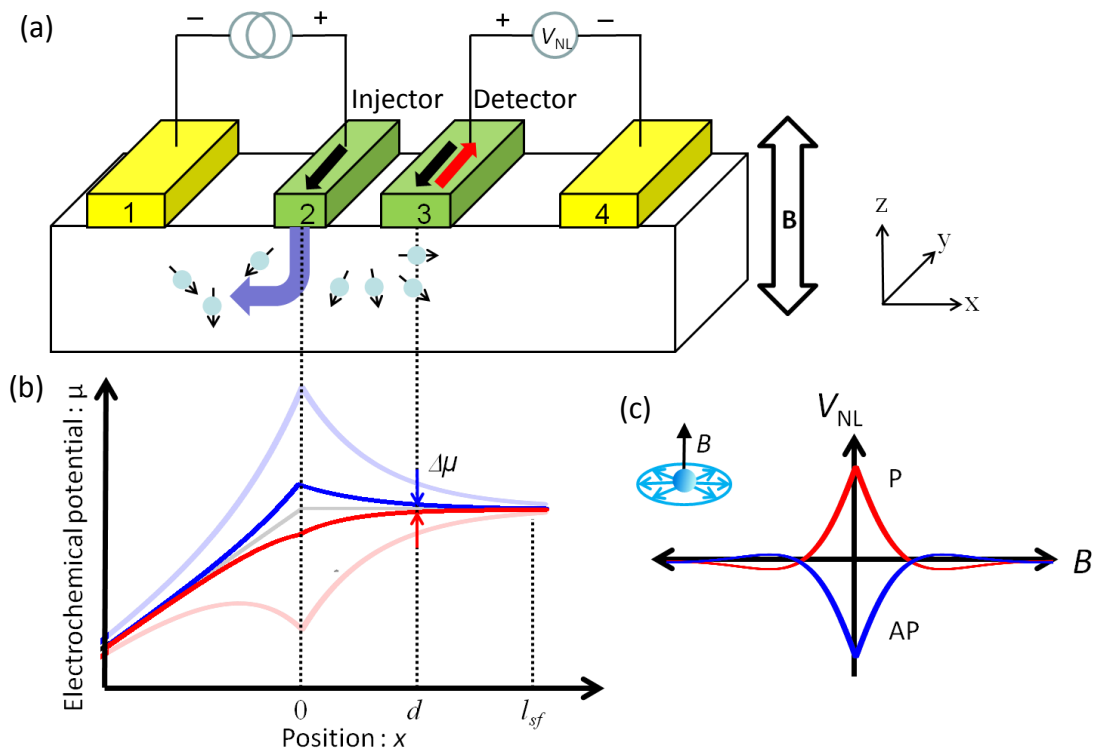


**Fig. 2.10.** Illustration of the Hanle effect including a) device structure and circuit configuration, b) electrochemical potential for up spin and down spin with a perpendicular magnetic field, and c) an example of a Hanle signal.

## 2.3 Detection of nuclear spins in a spin injection system

In this section, the principle of detection of the nuclear spins from the non-local voltage of the electron spins will be introduced. The non-local voltage is a measure of the response of the electron spins to the effective magnetic field including a static magnetic field and a nuclear field. Since the nuclear spins affect the electron spins as a nuclear field, any change in the nuclear spin state will lead to a change in the nuclear field, resulting in a change in  $V_{NL}$ . From the change in the non-local voltage  $\Delta V_{NL}$ , the nuclear spin state can be read out.

### 2.3.1 Nuclear field polarized by electron spins

The rate equation for dynamic nuclear polarization by spin-polarized electrons can be constructed from the balance of nuclear polarization and depolarization rates  $T_{1e}^{-1}$  and  $T_1^{-1}$  [10]:

$$\frac{d\langle I_z \rangle}{dt} = -\frac{1}{T_{1e}} \left[ \langle I_z \rangle - f \frac{I(I+1)}{s(s+1)} \langle S_z \rangle \right] - \frac{1}{T_1} \langle I_z \rangle, \quad (2.7)$$

where  $\langle I_z \rangle$  and  $\langle S_z \rangle$  are the average nuclear and electron spin along the applied magnetic field  $\mathbf{B}_0 = B_0 \hat{z}$ ,  $I$  and  $s$  are the quantum numbers of the nuclei and electrons, respectively, and  $f$  is the leakage factor. By solving this rate equation in steady state, the average nuclear spin  $\mathbf{I}_{av} = \langle I_z \rangle \hat{z}$  along the magnetic field is found to be

$$\mathbf{I}_{av} = f \frac{I(I+1)}{s(s+1)} \frac{\mathbf{B}_0 \cdot \mathbf{S}}{\mathbf{B}_0^2 + \xi \mathbf{B}_L^2} \mathbf{B}_0, \quad (2.8)$$

where  $\mathbf{S}$  is average electron spin ( $|\mathbf{S}| = 1/2$ , corresponding to 100% polarization), and

$\frac{T_{1e}}{T_1} = \xi \left( \frac{\mathbf{B}_L}{\mathbf{B}_0} \right)^2$  is used [10], where  $\xi$  is a numerical coefficient defined by the ratio

of the nuclear spin polarization rate to the depolarization rate, and  $\mathbf{B}_L$  is the local field experienced by the nuclei.

The average effect of the hyperfine interaction between an electron and all nuclei is an effective magnetic field [10, 11]

$$\mathbf{B}_n = b_n \mathbf{I}_{av} / I, \quad (2.9)$$

where  $b_n = \frac{16\pi}{3g\nu_0} \mu_l \eta N$  is the effective nuclear field at 100% nuclear polarization,

where  $g$  is the electron  $g$  factor ( $g = -0.44$  in GaAs),  $\nu_0$  is the volume of the unit cell,  $\mu_l$  is the nuclear magnetic moment,  $\eta$  is the electron wave function density, and  $N$  is the number of the nuclei in the unit cell. Interestingly, the nuclear field is anti-parallel to the average nuclear spin because of the negative electron  $g$  factor in GaAs.

Thus, the steady-state nuclear field is

$$\mathbf{B}_n = f b_n \frac{(I+1)}{s(s+1)} \frac{\mathbf{B}_0 \cdot \mathbf{S}}{\mathbf{B}_0^2 + \xi \mathbf{B}_L^2} \mathbf{B}_0. \quad (2.10)$$

The polarized nuclear spins affect electron spins as an effective magnetic field or Overhauser field. Thus, one can evaluate the degree of nuclear spin polarization through the strength of the Overhauser field. To detect the nuclear field, oblique Hanle effect measurements in which an oblique magnetic field is used have been widely used [12-18].

### 2.3.2 Detection of NMR from a non-local voltage of electron spins

To generate a nuclear field, an oblique magnetic field with respect to the electron spin direction is necessary because  $\mathbf{B}_n \propto \mathbf{B}_0 \cdot \mathbf{S}$ .  $\mathbf{S}$  is the average electron spin and it is in the direction of the  $x$ -axis at  $\mathbf{B}_0 = 0$ . According to Eq. (2.10), a nuclear field  $\mathbf{B}_n$  being antiparallel to the static magnetic field  $\mathbf{B}_0$  should be generated as shown in Fig. 2.11. Similarly to the conventional Hanle effect, the electron spins precess along the effective magnetic field of  $\mathbf{B}_0 + \mathbf{B}_n$ , and the non-local voltage  $V_{NL}$  can be described by Eq. (2.6) where  $B_z$  is the  $z$  component of the effective magnetic field.

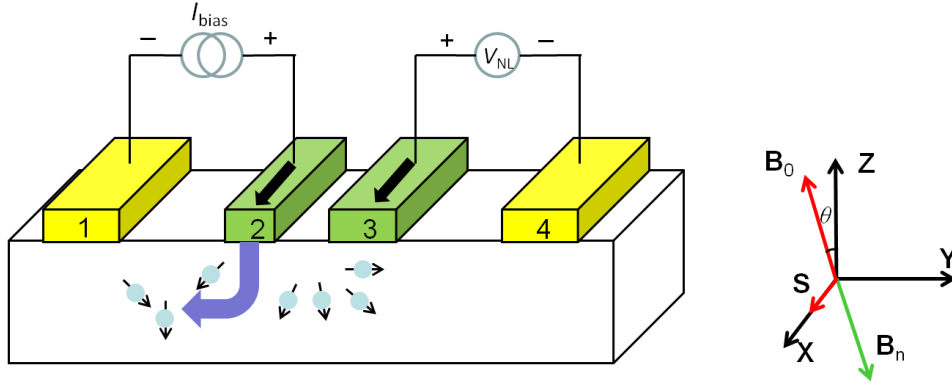


**Fig. 2.11.** The measurement configuration to generate a nuclear field with an oblique magnetic field.

Figure 2.12 shows the measurement flow of detection of nuclear spins through the detection of  $V_{\text{NL}}$ . First, the nuclear spins are initialized by the DNP process, and a nuclear field ( $\mathbf{B}_n$ ) being antiparallel to the static magnetic field ( $\mathbf{B}_0$ ) should be generated. The electron spins precess along the effective magnetic field ( $\mathbf{B}_0 + \mathbf{B}_n$ ), which is detected by  $V_{\text{NL}}$ . Then a pulse should be applied for the Rabi oscillation or spin-echo measurement. For example, in the case of spin-echo measurement, a spin-echo pulse is applied and the nuclear field is rotated by one circle. After the application of the pulse, the nuclear field decays ( $\mathbf{B}_n'$ ), resulting in a change ( $\Delta\mathbf{B}_n$ ) in the effective magnetic field. If the effective magnetic field is decreased (increased), the electron spin precession is suppressed (enhanced), leading to an increase (decrease) in the  $V_{\text{NL}}$ . Therefore, the nuclear spins manipulated by the NMR effect can be detected from the non-local voltage.

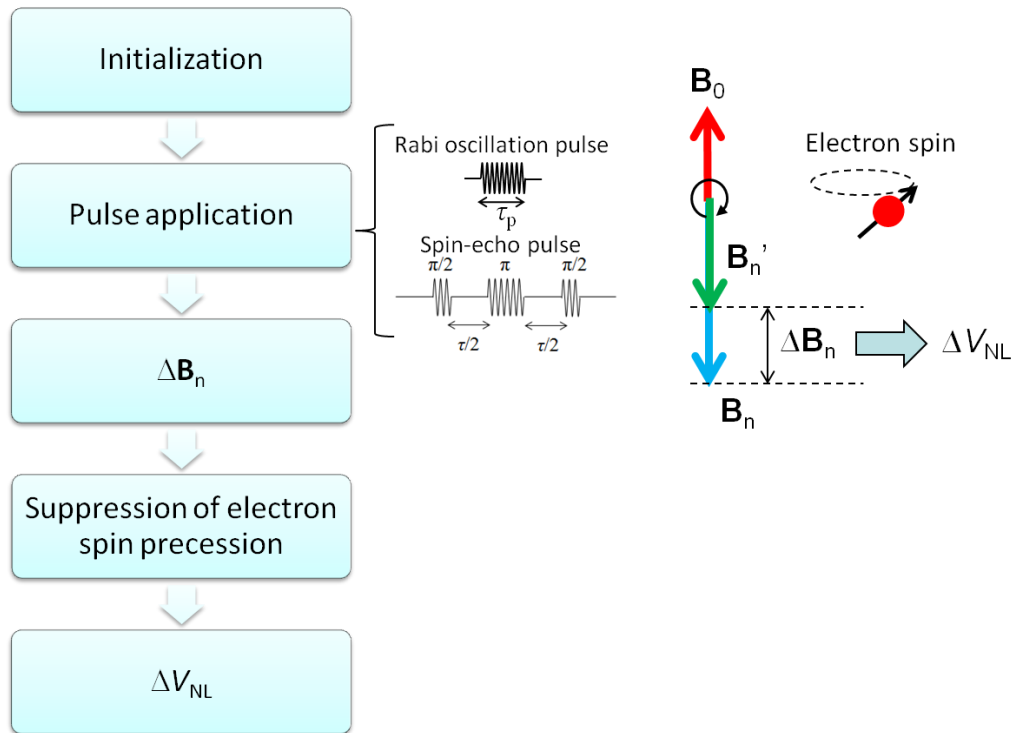


**Fig. 2.12.** Measurement flow of detection of nuclear spin through the non-local voltage  $V_{NL}$ .

## References

- [1] C. Kittel, in *Introduction to Solid State Physics*, ed. C. Kittel (Chemical Industry Press, Beijing, 2005), Chap. 13.
- [2] H. C. Torrey, *Phys. Rev.* **76**, 1059 (1949).
- [3] X. Lou, C. Adelman, S. A. Crooker, E. S. Garlid, J. Zhang, S. M. Reddy, S. D. Flexner, C. J. Palmstrøm, and P. A. Crowell, *Nat. Phys.* **3**, 197 (2007).
- [4] G. Salis, A. Fuhrer, R. R. Schlittler, L. Gross, and S. F. Alvarado, *Phys. Rev. B* **81**, 205323 (2010).
- [5] M. Ciorga, A. Einwanger, U. Wurstbauer, D. Schuh, W. Wegscheider, and D. Weiss, *Phys. Rev. B* **79**, 165321 (2009).
- [6] A. Fert and H. Jaffrès, *Phys. Rev. B* **64**, 184420 (2001).
- [7] T. Uemura, T. Akiho, M. Harada, K. -i. Matsuda, and M. Yamamoto, *Appl. Phys. Lett.* **99**, 082108 (2011).
- [8] I. Zutic, Jaroslav Fabian, S. D. Samra, *Rev. of Mod. Phys.* **76**, 323 (2004).
- [9] J. Fabian, A. Matos-Abiaguea, C. Ertlera, P. Stano, I. I. Zutic, *acta Phys. Slov.* **57**, 565 (2007).
- [10] J. Strand, X. Lou, C. Adelman, B. D. Schultz, A. F. Isakovic, C. J. Palmstrøm, and P. A. Crowell, *Phys. Rev. B* **72**, 155308 (2005).
- [11] M. I. Dyakonov and V. I. Perel, in *Optical Orientation*, ed. F. Meier and B. P. Zakharchenya (North-Holland, Amsterdam, 1984), Chap. 2.
- [12] M. I. Dyakonov, V. I. Perel, V. L. Berkovits, and V. I. Safarov, *Sov. Phys. JETP* **40**, 950 (1975).
- [13] J. Strand, X. Lou, C. Adelman, B. D. Schultz, A. F. Isakovic, C. J. Palmstrøm, and P. A. Crowell, *Phys. Rev. B* **72**, 155308 (2005).
- [14] P. Van Dorpe, W. Van Roy, J. De Boeck, and G. Borghs, *Phys. Rev. B* **72**, 035315 (2005).
- [15] M. K. Chan, Q. O. Hu, J. Zhang, T. Kondo, C. J. Palmstrøm, and P. A. Crowell, *Phys. Rev. B* **80**, 161206(R) (2009).
- [16] G. Salis, A. Fuhrer, and S. F. Alvarado, *Phys. Rev. B* **80**, 115332(R) (2009).

- [17] J. Shiogai, M. Ciorga, M. Utz, D. Schuh, T. Arakawa, M. Kohda, K. Kobayashi, T. Ono, W. Wegscheider, D. Weiss, and J. Nitta, *Appl. Phys. Lett.* **101**, 212402 (2012).
- [18] T. Akiho, J. Shan, H. -x. Liu, K. -i. Matsuda, M. Yamamoto, and T. Uemura, *Phys. Rev. B.* **87**, 235205 (2013).



# 3. Electrical spin injection into GaAs-based semiconductors with a highly polarized spin source

## 3.1 Introduction

The injection of spin-polarized electrons from ferromagnets into semiconductors has attracted much interest for creating spin transistors. Spin injection into bulk semiconductors such as Si [1,2] and Ge [3,4] has been realized using a four-terminal non-local geometry at room temperature. GaAs [5-7] also attracts much interest as a semiconductor material for spin injection because it has high electron mobility and abundant resources of nuclear spins in GaAs. Moreover, the two-dimensional electron gas (2DEG) structure of AlGaAs/GaAs has attracted much interest due to its higher electron mobility compared with bulk semiconductors, and it is used for high electron mobility transistors [8]. In addition, the 2DEG structure is useful as a channel of a spin transistor, and it has been suggested to employ Rashba spin-orbit interaction to controllably rotate the electron spins in a 2DEG channel via an electric field, which is well known as the Datta-Das spin transistor [9]. Up to now, the spin properties in 2DEGs have mostly been investigated using optical methods [10-12], and only a few reports on electrical spin injection are available [13-17]. Although electrical spin injection into an AlGaAs/GaAs 2DEG channel has been achieved by using GaMnAs as a spin source [16], the demonstration of spin injection was limited below 50 K because of the low Curie temperature ( $T_C < \sim 200$  K) of GaMnAs, which makes it difficult to investigate spin transport properties at a higher temperature.

Co-based Heusler alloys ( $\text{Co}_2\text{YZ}$ , where  $Y$  is usually a transition metal and  $Z$  is a main group element) are promising ferromagnetic electrode material because of the half metallicity and relatively high Curie temperatures (well above room temperature)

for some of them. Among them,  $\text{Co}_2\text{MnSi}$  (CMS) is one of the most extensively investigated ferromagnetic electrode materials [18-29] because of its theoretically predicted half-metallic nature with a large half-metal gap of 0.81 eV for its minority-spin band [30-32] and its high Curie temperature of 985 K [33]. In previous studies, we have experimentally shown that harmful defects in CMS thin films – i.e.  $\text{Co}_{\text{Mn}}$  antisites – can be suppressed by increasing the Mn composition [22-24,34-36]. We demonstrated high tunneling magnetoresistance (TMR) ratios of up to 1995% at 4.2 K and up to 354% at 290 K in magnetic tunnel junctions (MTJs) with Mn-rich CMS electrodes [23], indicating a high spin polarization of Mn-rich CMS. Thus, a Mn-rich CMS is a promising spin source material for achieving spin injection into GaAs-based semiconductors.

## 3.2 Spin injection into bulk GaAs

### 3.2.1 Layer structure and device geometry

The layer structures (Fig. 3.1(a)) consisting of (from the substrate side) a 250-nm-thick undoped GaAs buffer layer, a 2500-nm-thick  $n^-$ -GaAs channel layer, and a 30-nm-thick  $n^+$ -GaAs layer were grown by molecular beam epitaxy (MBE) method at 590 °C on semi-insulating GaAs (001) substrate. The doping concentration of the  $n^-$ -GaAs layer was  $3 \times 10^{16} \text{ cm}^{-3}$  and the doping concentration of the  $n^+$ -GaAs layer was  $5 \times 10^{18} \text{ cm}^{-3}$ . The role of the  $n^+$ -GaAs layer is to form a narrow Schottky tunnel barrier to avoid the conductance mismatch problem [37, 38]. Then the samples were capped with an arsenic protection layer and transported in air to an ultrahigh vacuum chamber capable of magnetron sputtering. After the arsenic cap was removed by heating the samples to 300 °C, a 1.3-nm-thick ultrathin CoFe layer and a 5-nm-thick  $\text{Co}_2\text{MnSi}$  layer were deposited by magnetron sputtering at room temperature and successively annealed *in situ* at 350 °C. The  $\text{Co}_2\text{MnSi}$  layer was deposited by cosputtering from a  $\text{Co}_2\text{MnSi}$  target and a Manganese target. The film composition of the  $\text{Co}_2\text{MnSi}$  film was chosen to be  $\text{Co}_2\text{Mn}_{1.30}\text{Si}_{0.88}$  to suppress

harmful  $\text{Co}_{\text{Mn}}$  antisites [22-24,34-36]. The ultrathin CoFe layer was inserted to suppress the diffusion of Mn atoms into GaAs [29]. Finally, a 5-nm-thick Ru cap layer was deposited using magnetron sputtering at room temperature. By using electron-beam lithography and Ar ion milling techniques, a lateral spin injection device was fabricated (Fig. 3.1(b)). To avoid parallel conduction in  $n^+$ -GaAs, the  $n^+$ -GaAs layer was etched away between the contacts. The device consists of a 10- $\mu\text{m}$ -wide channel, two ferromagnetic contacts and two nonmagnetic contacts. Contact 2 ( $1 \times 10 \mu\text{m}^2$ ) works as the injector and contact 3 ( $0.5 \times 10 \mu\text{m}^2$ ) works as the detector. Contact 1 and contact 4 are nonmagnetic and they work as references.

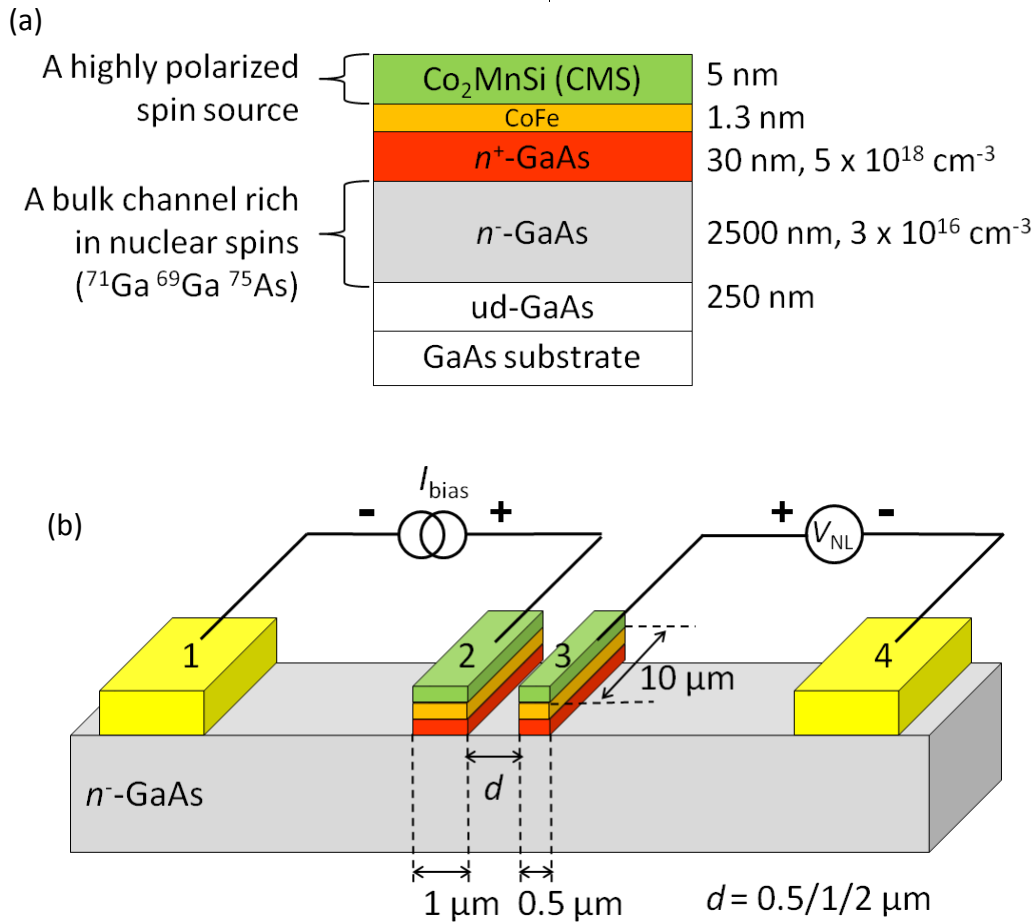


**Fig. 3.1.** (a) Layer structure of spin injection device. (b) Device structure and circuit configuration for non-local measurements.

### 3.2.2 Spin-valve signal and Hanle signal

Figure 3.2 shows (a) a spin-valve signal and (b) a Hanle signal measured in the spin injection device with  $\text{Co}_2\text{MnSi}/\text{CoFe}$  (1.3 nm)/n-GaAs structures at 4.2 K. In the spin-valve signal, a clear spin-valve-like behavior was observed at the magnetic field of  $\pm 9$  mT and  $\pm 18$  mT due to the switching between the parallel and anti-parallel states for the magnetization configuration between the injector and the detector. Furthermore, a dip structure was observed when the magnetic field became zero, indicating that the electron spins were depolarized. The origin of the dip structure was due to the nuclear spin polarization [28]. A clear Hanle signal was also observed with a parallel configuration, which was more rigorous evidence of spin injection. The estimated values of  $\tau_s$ ,  $l_{sf}$ , and the effective spin polarization defined by  $|P_{inj}P_{det}|^{1/2}$  in Eq. (2.6) were  $\tau_s = 20$  ns,  $l_{sf} = 3$   $\mu\text{m}$ , and  $|P_{inj}P_{det}|^{1/2} = \sim 30\%$ , respectively.

The experimentally observed spin-valve signal and Hanle signal indicate that electron spins are successfully injected into the spin injection device, and the highly polarized spin source of  $\text{Co}_2\text{MnSi}$  leads to a high electron spin polarization of  $\sim 30\%$ , which is promising for the dynamic nuclear polarization.

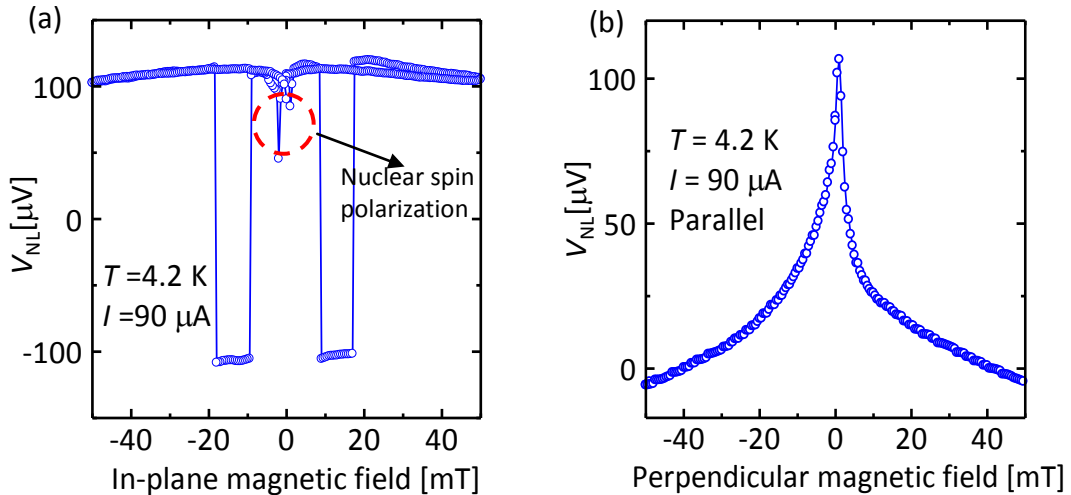


**Fig. 3.2.** (a) A spin-valve signal in which an in-plane magnetic field was swept. (b) A Hanle signal in which a perpendicular magnetic field was swept.

## 3.3 Spin injection into AlGaAs/GaAs heterostructures

### 3.3.1 Layer structure and device geometry

Figure 3.3(a) shows the layer structure of a spin injection device. Layers consisting of (from the substrate side) ud-GaAs (400 nm)/ud-Al<sub>0.3</sub>Ga<sub>0.7</sub>As (100 nm)/n<sup>-</sup>-Al<sub>0.3</sub>Ga<sub>0.7</sub>As (Si = 3-4 × 10<sup>18</sup> cm<sup>-3</sup> and 100 nm)/ud-Al<sub>0.3</sub>Ga<sub>0.7</sub>As (15 nm)/ud-GaAs (50 nm)/n<sup>-</sup>-GaAs (Si = 7 × 10<sup>16</sup> cm<sup>-3</sup> and 100 nm)/n<sup>+</sup>-GaAs (Si = 7.5-8.5 × 10<sup>18</sup> cm<sup>-3</sup> and 30 nm) were grown by molecular beam epitaxy (MBE) on a GaAs (001) substrate. Then a CoFe insertion layer (1.3 nm) and a CMS layer (5 nm) were grown by magnetron sputtering at room temperature and annealed at 400°C for 15 minutes. The purpose of the CoFe insertion layer is to prevent the diffusion of Mn atoms from the CMS into the GaAs [29]. For reference, a sample with a CoFe (5 nm,  $T_C > 1000$  K) spin source was also prepared. By using electron-beam lithography and Ar ion milling techniques, a lateral spin injection device was fabricated (Figure 3.3(b)). To avoid parallel conduction in bulk GaAs, the n<sup>+</sup>-GaAs layer was etched away between the contacts. The device consists of a 5-μm-wide channel, two ferromagnetic contacts and two nonmagnetic contacts. Contact 2 (1 × 10 μm<sup>2</sup>) works as the injector and contact 3 (0.5 × 10 μm<sup>2</sup>) works as the detector. Contact 1 and contact 4 are nonmagnetic and they work as references. The spacing ( $d$ ) between contact 2 and contact 3 is 0.5 or 1 or 2 μm. Hereafter, the device with a CMS spin source is referred to as CMS/2DEG, while the device with a CoFe spin source is referred to as CoFe/2DEG.

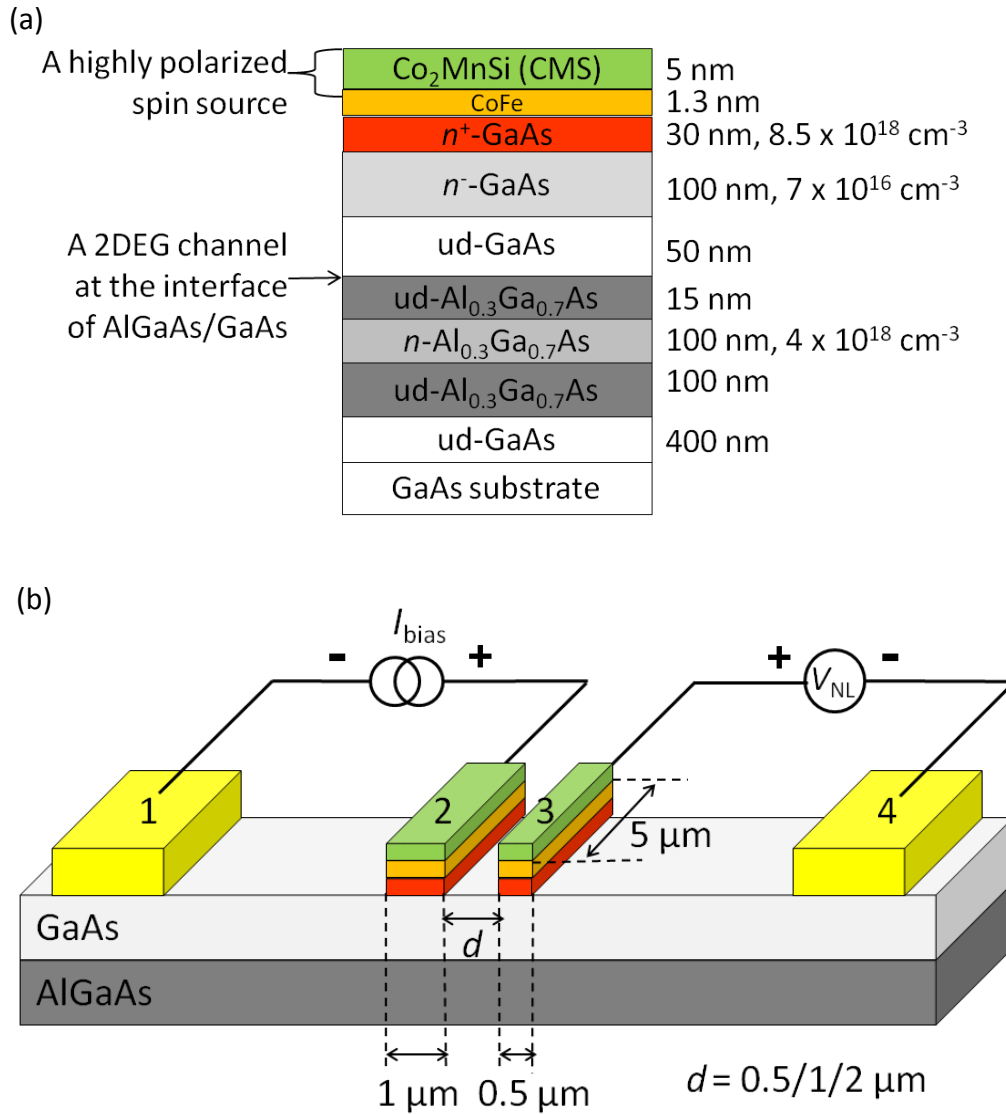


**Fig. 3.3.** (a) 2DEG layer structure of spin injection device. (b) Device structure and circuit configuration for non-local measurements.

## 3.3.2 Results and discussion

### 3.3.2.1 Mobility and contact resistance

From the Hall effect measurement, electron mobility ranging from 23,100 to 43,700  $\text{cm}^2/\text{V s}$  and sheet carrier concentration ranging from  $6.9 \times 10^{11}$  to  $8.5 \times 10^{11}$   $\text{cm}^{-2}$  were obtained at 77 K for the AlGaAs/GaAs 2DEG structures. Although samples with an identical layer structure were prepared, the result varies from sample to sample. The difference in the mobility probably results from the variation in the growth conditions such as the growth temperature [39]. Figure 3.4(a) shows the temperature dependence of the mobility for a 2DEG sample and a bulk GaAs sample. The mobility increases as temperature decreases for both samples until about 80 K. Then the mobility starts to decrease for the bulk sample while it keeps increasing for the 2DEG sample. This means that the ionized impurity scattering is suppressed at low temperature for the 2DEG sample. At 4.2 K, mobilities ranging from 32,400 to 80,500  $\text{cm}^2/\text{V s}$  were obtained. Such relatively high electron mobility indicates that the 2DEG channel was well formed at the interface of the AlGaAs/GaAs heterostructure. Figure 3.4(b) shows current density ( $J$ ) - voltage ( $V$ ) characteristics for the contacts of both the CoFe/2DEG and CMS/2DEG at 77 K. The nonlinear characteristics indicate the tunnel conduction through the Schottky barriers formed at the ferromagnet/semiconductor interfaces. The resistance-area product  $R_j A$ , where  $R_j$  is the junction resistance and  $A$  is a contact area, is  $400 - 100 \text{ k}\Omega \mu\text{m}^2$  for the CMS/2DEG and  $300 - 60 \text{ k}\Omega \mu\text{m}^2$  for the CoFe/2DEG at the temperatures ranging from 4.2 to 294 K. The spin resistance of the 2DEG channel defined by  $R_s l_{sf} W$  [38], where  $R_s$  is the sheet resistance of the channel,  $l_{sf}$  is the spin diffusion length (approx.  $2 \mu\text{m}$  or less, as shown later in Fig. 3.6(b)), and  $W$  ( $0.5$  or  $1.0 \mu\text{m}$ ) is the width of the contact along the channel direction, is  $0.6 - 2.5 \text{ k}\Omega \mu\text{m}^2$ . Thus, the values of  $R_j A$  are at least 24 times larger than those of  $R_s l_{sf} W$ , indicating that the spin absorption into ferromagnetic contact is negligible and that the spin injection efficiency is independent on  $R_j$ .

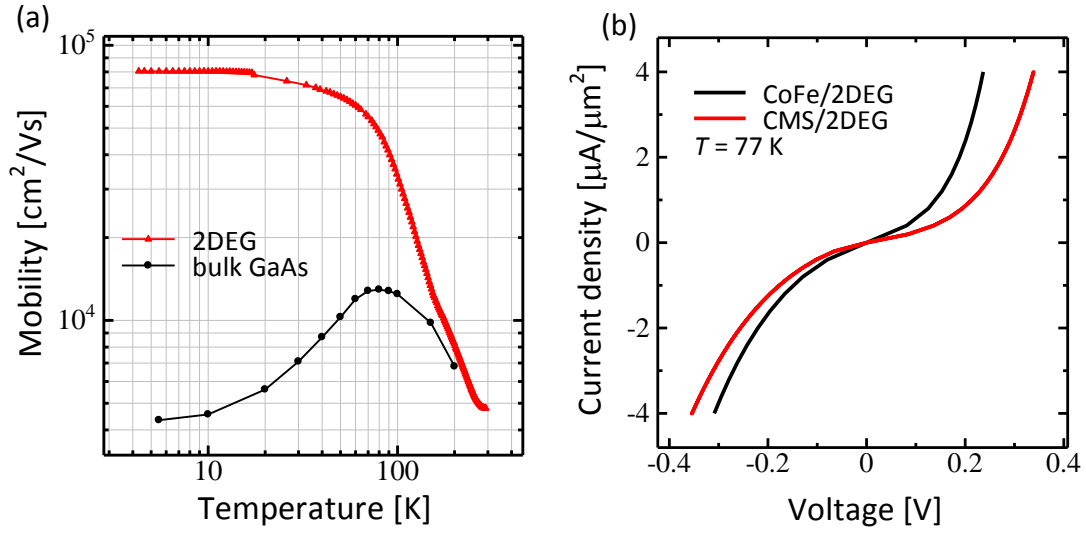


**Fig. 3.4.** (a) Temperature dependence of electron mobility for 2DEG sample and bulk GaAs sample. (b) Current density ( $J$ ) - voltage ( $V$ ) characteristic for the contacts of both the CoFe/2DEG and CMS/2DEG at 77 K.

### 3.3.2.2 Temperature dependence of spin-valve signal

Figure 3.5(a) shows a clear non-local spin-valve signal observed from the CMS/2DEG device at room temperature, a higher temperature than that reported in the previous study, which used GaMnAs as a spin source [16]. In contrast, no clear spin-valve signal was observed from the CoFe/2DEG device at room temperature due to the relatively large noise. Figure 3.5(b) shows the  $|\Delta V_{\text{NL}}|$  as a function of  $I_{\text{bias}}$  for both the CoFe/2DEG device and the CMS/2DEG device, where  $\Delta V_{\text{NL}} = V_{\text{NL}}^{\text{P}} - V_{\text{NL}}^{\text{AP}}$  is the amplitude of a spin-valve signal at 77 K. The nonlinear relations between  $|\Delta V_{\text{NL}}|$  and  $I_{\text{bias}}$  indicate that the value of  $(P_{\text{inj}}P_{\text{det}})^{1/2}$  is not constant against the bias voltage. Although there have been several experimental [5-6,28-29,40] and theoretical [41-43] investigations in which the magnitude and sign of the spin polarization for a ferromagnet/GaAs heterojunction are affected by the bias condition and/or ferromagnetic materials, the origin is still an open question. Importantly, compared with the CoFe/2DEG device, the  $|\Delta V_{\text{NL}}|$  of the CMS/2DEG device is about

2 times larger at positive bias, while it is 7-9 times larger at negative bias. It is noted that although the values of  $R_j$  differ between CMS/2DEG and CoFe/2DEG, as shown in Fig. 3.4(b), this effect cannot explain the difference of  $|\Delta V_{\text{NL}}|$ , because  $R_j A \gg R_s l_{\text{sf}} W$  is satisfied. The estimated spin polarization defined as  $(P_{\text{inj}} P_{\text{det}})^{1/2}$  in Eq. (2.5) for the CMS/2DEG device and the CoFe/2DEG device are about 12% and 5%, respectively, indicating a higher spin polarization for the CMS/2DEG device than for the CoFe/2DEG. However, the value of 12% for the CMS/2DEG is still less than the highest value of 52% ever reported in our previous study using a similar CMS spin source [29]. In the previous study, we found that the insertion of ultrathin CoFe between CMS and GaAs effectively suppressed the Mn diffusion from CMS into GaAs, but the spin polarization was so sensitive to the thickness of CoFe. Thus, the relatively low spin polarization obtained in the CMS/2DEG device is probably due to the insufficient optimization of the CoFe thickness.

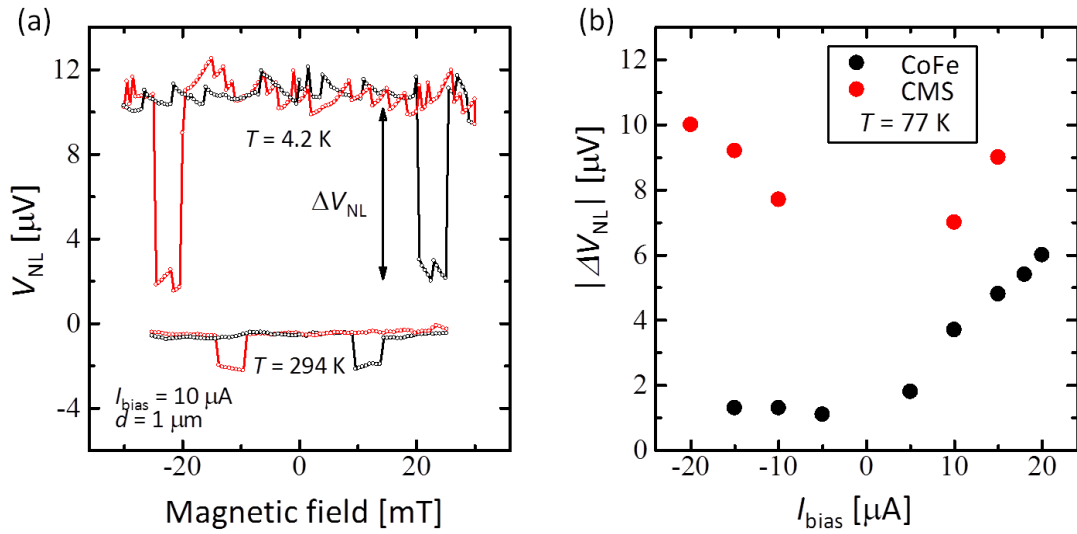


**Fig. 3.5.** (a) Non-local spin-valve signal observed at 4.2 K and 294 K for  $I_{\text{bias}} = 10 \mu\text{A}$  and  $d = 1 \mu\text{m}$  for a CMS/2DEG device with offset. Amplitude of spin-valve signal is defined as  $\Delta V_{\text{NL}} = V_{\text{NL}}^{\text{P}} - V_{\text{NL}}^{\text{AP}}$ . (b) Bias current dependence of  $|\Delta V_{\text{NL}}|$  for CMS/2DEG device and CoFe/2DEG device at 77 K.

Next, we describe the temperature dependence of the spin-valve signal. Figure 3.6(a) shows the  $|\Delta V_{\text{NL}}/I_{\text{bias}}|$  as a function of temperature for the CMS/2DEG device, the CoFe/2DEG device, and a bulk GaAs channel with a CoFe spin source [6], respectively. The details of the bulk GaAs channel has been presented elsewhere [6], and it is referred to as CoFe/GaAs hereafter. The spin-valve signal was observed up to room temperature for the CMS/2DEG device and the CoFe/GaAs device, while for the CoFe/2DEG device, the spin-valve signal disappeared after about 140 K. One reason for the disappearance of the spin-valve signal is the relatively large channel resistance in CoFe/2DEG compared with that in CoFe/GaAs. Above 100 K, the sheet resistance of CoFe/2DEG is about 10 times larger than that of CoFe/GaAs, which leads to relatively large noise in CoFe/2DEG. Another reason is the quick increase in the background signal of CoFe/2DEG as the temperature continuously increases above 100 K, making it difficult to distinguish the spin-valve signal. The origin of the background signal is not fully understood yet but it may be related to the sheet resistance because a quick increase in the sheet resistance of CoFe/2DEG above 100 K was observed while it is smaller for CoFe/GaAs. Interestingly, for both the 2DEG devices, the spin-valve signal does not show a monotonic decrease with increasing temperature, and it reaches a peak at about 80 K. This contrasts with the result observed in bulk GaAs [6], in which a monotonic decrease of spin-valve signals with increasing temperature was observed. To analyze this behavior, the parameters in Eq. (2.5) were estimated for the CMS/2DEG device. Figure 3.6(b) shows the temperature dependence of the spin diffusion length  $l_{\text{sf}}$  and the effective spin polarization  $(P_{\text{inj}}P_{\text{det}})^{1/2}$ , which were estimated from the spacing ( $d$ ) dependence of the spin-valve signal. The spin diffusion length at 4.2 K is about 2.5  $\mu\text{m}$ , which is comparable with that in the previous study [16]. And this value is also comparable with that in bulk GaAs [5,6]. As the temperature increases,  $l_{\text{sf}}$  decays and becomes about 1  $\mu\text{m}$  at room temperature. For the spin polarization, it does not decrease but increases slightly as the temperature increases from 4.2 K to 100 K. This kind of abnormal behavior has been reported in a previous study in Fe/GaAs structures [5], in which  $|P_{\text{inj}}P_{\text{det}}|$  rises with increasing temperature between 30 and 140 K. And they argue that such

behavior is likely associated with an increase in minority spin injection through the resonant state formed at Fe/GaAs interface. As the temperature increases, the energy of the electrons increases and comes closer to the resonant level, resulting in an increase in the minority-spin injection efficiency [42]. Similar mechanism may happen in our device at temperature below 100 K. As the temperature increases above 100 K, the spin polarization quickly drops to about 4% and remains almost unchanged up to room temperature. Figure 3.6(b) also shows the sheet resistance  $R_s$  for the 2DEG device and the bulk GaAs device, which were estimated from the Hall effect measurement. Note that below 100 K, the  $R_s$  for the 2DEG device and the bulk GaAs device show opposite tendencies with increasing temperature. From the analysis, we found that from 4.2 K to about 100 K, although  $l_{sf}$  decreases as the temperature increases,  $(P_{inj}P_{det})^{1/2}$  and  $R_s$  increase, which maintains the magnitude of the spin-valve signal. However, the  $R_s$  of bulk GaAs decreases in this temperature range, resulting in a different temperature dependence behavior of the spin-valve signal compared with that of the 2DEG device. More importantly, the spin-valve signal in the CMS/2DEG device decreases by a factor of about 5.6 with increasing temperature from 4.2 K to 294 K, and this factor is smaller than the values reported in bulk GaAs devices [5-7,29]. This result suggests that the spin-valve signal in a 2DEG device is less sensitive to temperature than that in a bulk device.

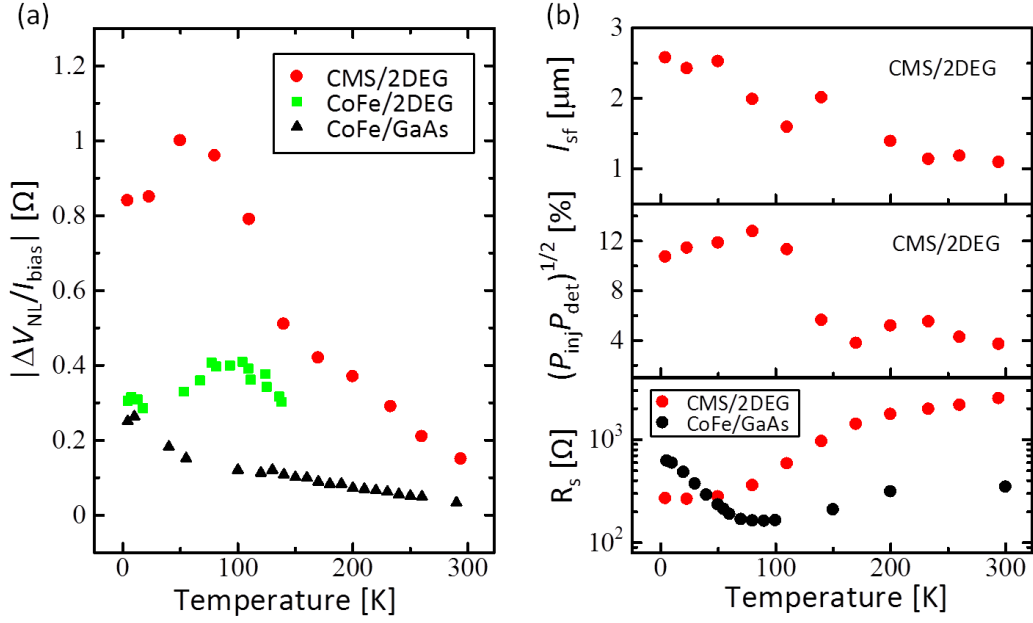


**Fig. 3.6.** (a) Temperature dependence of  $|\Delta V_{NL}/I_{bias}|$  for CMS/2DEG device, CoFe/2DEG device, and CoFe/GaAs device, respectively. (b) Parameters estimated in Eq. (2.5) for CMS/2DEG device. Spin diffusion length  $l_{sf}$  and spin polarization  $(P_{inj}P_{det})^{1/2}$  were estimated from spacing ( $d$ ) dependence of spin-valve signal. Sheet resistance  $R_s$  for 2DEG device and bulk GaAs device were estimated from Hall effect measurement.

### 3.3.2.3 Spin lifetime

Although the observation of a Hanle signal is more rigorous evidence of spin injection, no clear Hanle signal was observed in our device due to a relatively large background signal. The relatively small spin lifetime [16,44-45] also makes it difficult to observe the Hanle precession. To understand the spin relaxation mechanism in the 2DEG device, the spin lifetime was estimated by

$$\tau_s = l_{sf}^2 / D, \quad (3.1)$$

where  $l_{sf}$  is the spin diffusion length, and  $D = 1/[e^2 g(E_F) R_s]$  is the diffusion constant, where  $e$  is the electron charge,  $g(E_F)$  is the density of states at the Fermi level, and  $R_s$  is the sheet resistance. Figure 3.7 shows the temperature dependence of

the spin lifetime, which was found to be weakly dependent on the temperature. Such weak temperature dependence of  $\tau_s$  was also reported in AlGaAs/GaAs quantum wells in the range of 90-300 K, and this was investigated by optical methods [45]. The D'yakonov-Perel' mechanism is expected to be the spin relaxation mechanism for the AlGaAs/GaAs heterostructure and it predicts [44]

$$1/\tau_s \propto T\tau_p, \quad (3.2)$$

for a narrow quantum well, where  $T$  is the temperature and  $\tau_p$  is the momentum scattering time. Figure 3.7 also plots the temperature dependence of the product of  $T$  and  $\tau_p$ . From about 100 K to room temperature,  $T\tau_p$  is almost constant, which is consistent with the constant  $\tau_s$ . Therefore, the spin relaxation mechanism should be the D'yakonov-Perel' mechanism. However, below about 100 K, although  $\tau_s$  stays constant,  $T\tau_p$  shows strong temperature dependence, which breaks the relation of Eq. (3.2). Another mechanism that might be related is the Elliott-Yafet mechanism, which predicts [46]

$$1/\tau_s \propto T/\tau_p. \quad (3.3)$$

However,  $T/\tau_p$  shows a similar tendency to that of  $T\tau_p$  below about 100 K as shown in Fig. 3.7. Thus, it is impossible to explain the spin relaxation by D'yakonov-Perel' and/or Elliott-Yafet mechanism, and further studies are needed to clarify the mechanism in this temperature range.

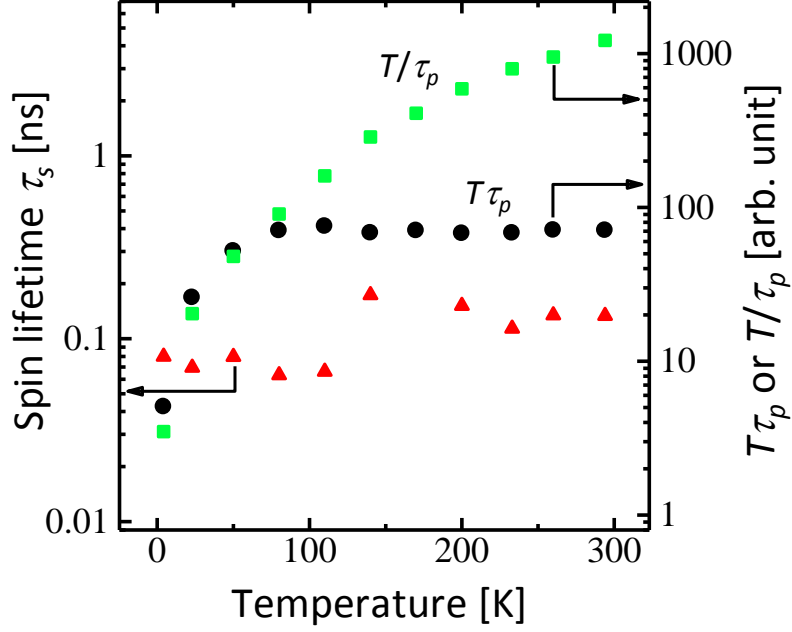


**Fig. 3.7.** Temperature dependence of spin lifetime  $\tau_s$  (left-axis and red triangles), product of  $T\tau_p$  (right-axis and black circles) that corresponds to D'yakonov-Perel' mechanism, and  $T/\tau_p$  (right-axis and green circles) that corresponds to Elliott-Yafet mechanism, where  $T$  is temperature and  $\tau_p$  is momentum scattering time, which was estimated from Hall measurement result.

### 3.4 Summary and conclusion

In summary, electrical spin injection was demonstrated into bulk GaAs and AlGaAs/GaAs heterostructures using  $\text{Co}_2\text{MnSi}$  as a spin source.

In bulk GaAs, a clear spin-valve signal and a Hanle signal were observed. The highly polarized spin source of  $\text{Co}_2\text{MnSi}$  resulted in a high spin polarization, which is promising for the DNP process. Moreover, an indication of nuclear spin polarization was observed in the spin-valve signal at zero magnetic field.

In the AlGaAs/GaAs heterostructure, a spin-valve signal was observed up to room temperature. The spin-valve signal regarding the temperature shows relatively complicated behavior compared with that of the bulk device, which results from the opposite tendency of sheet resistance. Moreover, the spin-valve signal in the 2DEG

device is less sensitive to temperature than that in the bulk device. This result contributes to a better understanding of spin transport in a 2DEG channel, which is indispensable for realizing future spin transistors that can operate at room temperature.

Table 3.1 shows the comparison between bulk GaAs and AlGaAs/GaAs heterostructures. Bulk GaAs has higher spin polarization and longer spin lifetime, which are necessary for efficient DNP. Moreover, an indication of nuclear spin polarization was observed in the spin-valve signal from bulk GaAs, which however, was not observed from AlGaAs/GaAs heterostructures. In conclusion, the bulk GaAs device is suitable for investigating the nuclear spins.

**Table 3.1.** Comparison between bulk GaAs and AlGaAs/GaAs 2DEG.

$T = 4.2$ K	Bulk GaAs	AlGaAs/GaAs
Spin polarization	~30%	~10%
Spin lifetime	~20 ns	~0.1 ns
Spin-valve signal	Yes	Yes
Nuclear spin polarization in spin-valve signal	Yes	No
Hanle signal	Yes	No

## References

- [1] T. Suzuki, T. Sasaki, T. Oikawa, M. Shiraishi, Y. Suzuki, and K. Noguchi, *Appl. Phys. Express* **4**, 023003 (2011).
- [2] A. Tiwari, T. Inokuchi, M. Ishikawa, H. Sugiyama, N. Tezuka, and Y. Saito, *Jpn. J. Appl. Phys.* **56**, 04CD05 (2017).
- [3] F. Rortais, C. Vergnaud, A. Marty, L. Vila, J.-P. Attané, J. Widiez, C. Zucchetti, F. Bottegoni, H. Jaffrès, J.-M. George, and M. Jamet, *Appl. Phys. Lett.* **111**, 182401 (2017).
- [4] M. Yamada, M. Tsukahara, Y. Fujita, T. Naito, S. Yamada, K. Sawano, and K. Hamaya, *Appl. Phys. Express* **10**, 093001 (2017).
- [5] G. Salis, A. Fuhrer, R. R. Schlittler, L. Gross, and S. F. Alvarado, *Phys. Rev. B* **81**, 205323 (2010).
- [6] T. Uemura, T. Akiho, M. Harada, K.-i. Matsuda, and M. Yamamoto, *Appl. Phys. Lett.* **99**, 082108 (2011).
- [7] T. A. Peterson, S. J. Patel, C. C. Geppert, K. D. Christie, A. Rath, D. Pennachio, M. E. Flatte, P. M. Voyles, C. J. Palmstrøm, and P. A. Crowell, *Phys. Rev. B* **94**, 235309 (2016).
- [8] T. Mimura, *Jpn. J. Appl. Phys.* **44**, 8263 (2005).
- [9] S. Datta and B. Das, *Appl. Phys. Lett.* **56**, 665 (1990).
- [10] C. P. Weber, N. Gedik, J. E. Moore, J. Orenstein, J. Stephens, and D. D. Awschalom, *Nature (London)* **437**, 1330 (2005).
- [11] D. Stich, J. Zhou, T. Korn, R. Schulz, D. Schuh, W. Wegscheider, M. W. Wu, and C. Schüller, *Phys. Rev. Lett.* **98**, 176401 (2007).
- [12] T. Korn, *Phys. Rep.* **494**, 415 (2010).
- [13] A. T. Filip, B. H. Hoving, F. J. Jedema, B. J. van Wees, B. Dutta, and S. Borghs, *Phys. Rev. B* **62**, 9996 (2000).
- [14] P. R. Hammar and M. Johnson, *Phys. Rev. Lett.* **88**, 066806 (2002).
- [15] H. C. Koo, J. H. Kwon, J. Eom, J. Chang, and M. Johnson, *Science* **325**, 1515 (2009).

- [16] M. Oltscher, M. Ciorga, M. Utz, D. Schuh, D. Bougeard, and D. Weiss, *Phys. Rev. Lett.* **113**, 236602 (2014).
- [17] T. Ishikura, L-K. Liefeth, Z. Cui, K. Konishi, K. Yoh, and T. Uemura, *Appl. Phys. Express* **7**, 073001 (2014).
- [18] S. Kämmerer, A. Thomas, A. Hütten, and G. Reiss, *Appl. Phys. Lett.* **85**, 79 (2004).
- [19] Y. Sakuraba, M. Hattori, M. Oogane, Y. Ando, H. Kato, A. Sakuma, T. Miyazaki, and H. Kubota, *Appl. Phys. Lett.* **88**, 192508 (2006).
- [20] T. Ishikawa, T. Marukame, H. Kijima, K.-i. Matsuda, T. Uemura, M. Arita, and M. Yamamoto, *Appl. Phys. Lett.* **89**, 192505 (2006).
- [21] T. Ishikawa, H.-x. Liu, T. Taira, K.-i. Matsuda, T. Uemura, and M. Yamamoto, *Appl. Phys. Lett.* **95**, 232512 (2009).
- [22] M. Yamamoto, T. Ishikawa, T. Taira, G.-f. Li, K.-i. Matsuda, and T. Uemura, *J. Phys.: Condens. Matter* **22**, 164212 (2010).
- [23] H.-x. Liu, Y. Honda, T. Taira, K.-i. Matsuda, M. Arita, T. Uemura, and M. Yamamoto, *Appl. Phys. Lett.* **101**, 132418 (2012).
- [24] G.-f. Li, Y. Honda, H.-x. Liu, K.-i. Matsuda, M. Arita, T. Uemura, M. Yamamoto, Y. Miura, M. Shirai, T. Saito, F. Shi, and P. M. Voyles, *Phys. Rev. B* **89**, 014428 (2014).
- [25] B. Hu, K. Moges, Y. Honda, H.-x. Liu, T. Uemura, and M. Yamamoto, *Phys. Rev. B* **94**, 094428 (2016).
- [26] K. Yakushiji, K. Saito, S. Mitani, K. Takanashi, Y. K. Takahashi, and K. Hono, *Appl. Phys. Lett.* **88**, 222504 (2006).
- [27] Y. Sakuraba, K. Izumi, T. Iwase, S. Bosu, K. Saito, K. Takanashi, Y. Miura, K. Futatsukawa, K. Abe, and M. Shirai, *Phys. Rev. B* **82**, 094444 (2010).
- [28] T. Akiho, J. Shan, H.-x. Liu, K.-i. Matsuda, M. Yamamoto, and T. Uemura, *Phys. Rev. B* **87**, 235205 (2013).
- [29] Y. Ebina, T. Akiho, H.-x. Liu, M. Yamamoto, and T. Uemura, *Appl. Phys. Lett.* **104**, 172405 (2014).

- [30] S. Ishida, S. Fujii, S. Kashiwagi, and S. Asano, *J. Phys. Soc. Jpn* **64**, 2152 (1995).
- [31] S. Picozzi, A. Continenza, and A. J. Freeman, *Phys. Rev. B* **66**, 094421 (2002).
- [32] I. Galanakis, P. H. Dederichs, and N. Papanikolaou, *Phys. Rev. B* **66**, 174429 (2002).
- [33] P. J. Webster, *J. Phys. Chem. Solids* **32**, 1221 (1971).
- [34] H. -x. Liu, T. Kawami, K. Moges, T. Uemura, M. Yamamoto, F. Shi, and P. M. Voyles, *J. Phys. D: Appl. Phys.* **48**, 164001 (2015).
- [35] J. -P. Wüstenberg, R. Fetzter, M. Aeschlimann, M. Cinchetti, J. Minář, Jürgen Braun, H. Ebert, T. Ishikawa, T. Uemura, and M. Yamamoto, *Phys. Rev. B* **85**, 064407 (2012).
- [36] V. R. Singh, V. K. Verma, K. Ishigami, G. Shibata, T. Kadono, A. Fujimori, D. Asakura, T. Koide, Y. Miura, M. Shirai, G. -f. Li, T. Taira, and M. Yamamoto, *Phys. Rev. B* **86**, 144412 (2012).
- [37] G. Schmidt, D. Ferrand, L. Molenkamp, A. T. Filip, and B. J. van Wees, *Phys. Rev. B* **62**, R4790 (2000).
- [38] A. Fert and H. Jaffrès, *Phys. Rev. B* **64**, 184420 (2001).
- [39] N. M. Cho, D. J. Kim, and A. Madhukar, *Appl. Phys. Lett.* **52**, 24 (1988).
- [40] X. Lou, C. Adelman, S. A. Crooker, E. S. Garlid, J. Zhang, K. S. M. Reddy, S. D. Flexner, C. J. Palmstrøm, and P. A. Crowell, *Nat. Phys.* **3**, 197 (2007).
- [41] H. Dery and L. J. Sham, *Phys. Rev. Lett.* **98**, 046602 (2007).
- [42] A. N. Chantis, K. D. Belashchenko, D. L. Smith, E. Y. Tsybal, M. van Schilfgaarde, and R. C. Albers, *Phys. Rev. Lett.* **99**, 196603 (2007).
- [43] S. Honda, H. Itoh, and J. Inoue, *J. Phys. D: Appl. Phys.* **43**, 135002 (2010).
- [44] I. Zutic, J. Fabian, and S. D. Samra, *Rev. Mod. Phys.* **76**, 323 (2004).
- [45] A. Malinowski, R. S. Britton, T. Grevatt, and R. T. Harley, *Phys. Rev. B* **62**, 13034 (2000).
- [46] A. Tackeuchi, T. Kuroda, S. Muto, Y. Nishikawa, and O. Wada, *Jpn. J. Appl. Phys.* **38**, 4680 (1999).

# 4. Transient analysis of dynamic nuclear polarization

## 4.1 Introduction

As introduced in section 2.3, an oblique magnetic field is necessary to generate a nuclear field, and oblique Hanle effect measurements are used to detect the nuclear field. An oblique Hanle effect measurement is similar with the conventional Hanle effect measurement except that an oblique magnetic field is swept. Figure 4.1(a) shows a simulation result of a steady-state oblique Hanle signal, in which the nuclear field is calculated by using Eq. (2.10). It is asymmetric with respect to the polarity of the magnetic field by the following reason. When  $\mathbf{B} \cdot \mathbf{S} > 0$ , according to Eq. (2.10), the nuclear field  $\mathbf{B}_n$  is anti-parallel to the external magnetic field. Since the Hanle precession is induced by the total magnetic field of  $\mathbf{B} + \mathbf{B}_n$ , when  $\mathbf{B}$  and  $\mathbf{B}_n$  cancel each other, the Hanle precession is suppressed, resulting in a side peak. On the other hand, when  $\mathbf{B} \cdot \mathbf{S} < 0$ , the nuclear field is parallel to the external magnetic field. Thus, no cancellation can occur. To ensure that the nuclear spins are in steady states, the magnetic field has to be swept slowly enough because the DNP process takes several hundred seconds or more.

Figure 4.1(b) shows a typical transient oblique Hanle signal measured in the spin injection device with  $\text{Co}_2\text{MnSi}/\text{CoFe}$  (1.1 nm)/n-GaAs structures at 4.2 K. Because the magnetic field was swept (0.18 mT/s) faster than the DNP process, the behavior of the nuclear spins became complicated. Compared with the steady-state oblique Hanle signal (Fig. 4.1(a)), we experimentally observed the following two features: (1) an additional side peak was observed in the negative sweep direction, and (2) no side peak was observed in the positive sweep direction, showing a clear hysteretic nature depending on the sweep direction.

To explain these behaviors of the nuclear spins, we introduce the nuclear spin

temperature because the DNP process can be described by the time evolution of the nuclear spin temperature. To fully exploit the nuclear spins in future spintronics, we quantitatively analyze the transient response of nuclear spins to a change in the magnetic field in the DNP process by using the concept of nuclear spin temperature.

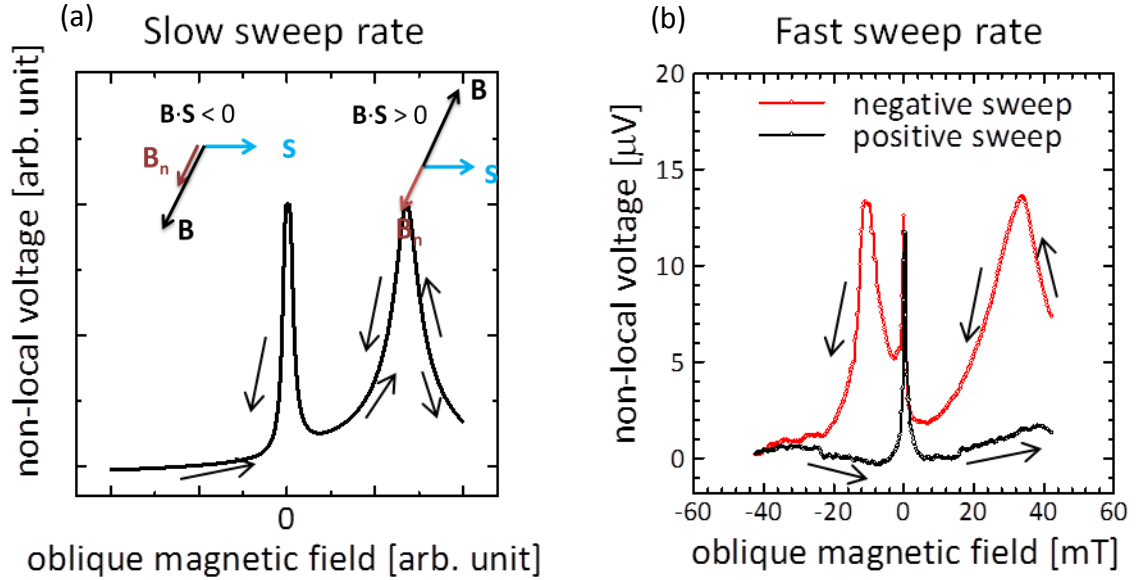


**Fig. 4.1.** (a) A simulation result of a steady-state oblique Hanle signal with a slow sweep rate.

(b) A typical transient oblique Hanle signal observed in GaAs with a fast sweep rate.

## 4.2 Simulation model

### 4.2.1 Nuclear spin temperature

Nuclear spins are coupled to each other by spin-spin interactions, and also loosely coupled to a lattice by a spin-lattice relaxation mechanism. The time scale for the spin-lattice system to reach thermodynamic equilibrium is characterized by  $T_1$ , which is on the order of 1 s or more. On the other hand, the interactions inside the nuclear spin system (dipole-dipole interaction of the nuclear magnetic moments) are characterized by a much shorter time,  $T_2$ . Each of the nuclei experiences a fluctuating local field  $B_L$  generated by its neighbors. The period of the nuclear spin precession in

$B_L$  defines the characteristic time of the interactions inside the nuclear spin system. Owing to these internal interactions, the nuclear spin system reaches the thermodynamic equilibrium internally during a time of order of  $T_2$ , which is given by  $1/\gamma B_L$  and is generally on the order of 100  $\mu\text{s}$ , where  $\gamma$  is the gyromagnetic ratio of nuclei. This equilibrium state is characterized by a nuclear spin temperature [1] which in general differs strongly from the lattice temperature because  $T_1 \gg T_2$ .

Figure 4.2(a) shows a two-level nuclear spin system in the presence of an external magnetic field. According to the fundamental Boltzmann law of statistical mechanics, the populations  $P_i$  with the energy levels  $E_i$  are proportional to  $\exp(-E_i/k_B\theta)$ , where  $k_B$  is the Boltzmann constant and  $\theta$  is the nuclear spin temperature. The net magnetization of a sample containing  $N$  spins will thus be [2]

$$M = N\gamma\hbar \frac{\sum_{m=-I}^I m \exp(\gamma\hbar mB / k_B\theta)}{\sum_{m=-I}^I \exp(\gamma\hbar mB / k_B\theta)} \quad (4.1)$$

$$= \frac{N\gamma^2\hbar^2 I(I+1)}{3k_B\theta} B.$$

So the average nuclear spin will be

$$I_{av} = \frac{M}{N\gamma\hbar} = \frac{(I+1)\mu_I}{3k_B\theta} B. \quad (4.2)$$

This is the well-known Curie's law. Since the nuclear magnetic moment is three orders smaller than that of the electron magnetic moment, it is very difficult to detect the nuclear spins by conventional magnetostatic methods. From this point of view, the DNP has attracted much interest because it can drastically increase the average nuclear spin by decreasing the nuclear spin temperature.

## 4.2.2 Cooling of the nuclear spin system through the DNP process

In the presence of polarized electrons, nuclear spins are effectively polarized through the transfer of spin angular momentum from polarized electrons to nuclei, leading to the decrease in nuclear spin temperature. The sign of the nuclear spin temperature is positive (negative) when the sign of  $\mathbf{B} \cdot \mathbf{S}$  is positive (negative). In the case that  $\mathbf{B} \cdot \mathbf{S}$  is positive (Fig. 4.2(b)), the spin angular momentum parallel to  $\mathbf{B}$  is transferred into the nuclear spin system, leading to an increased nuclear spin polarization. This corresponds to cooling of the nuclear spin temperature below the lattice temperature. For example, for  $|\mathbf{S}| = 0.25$  and  $|\mathbf{B}| = 5$  mT, one finds  $\theta \sim 10^{-6}$  K. When  $\mathbf{B} \cdot \mathbf{S}$  is negative (Fig. 4.2(c)), on the other hand, nuclear spins are negatively polarized because a population inversion occurs through the transfer of spin angular momentum antiparallel to  $\mathbf{B}$ , and the nuclear spin temperature becomes negative. However, the picture described above is the one for steady-state nuclear spins. If the external magnetic field is changed faster than the time scale of the DNP, the transient response of nuclear spins should be considered.

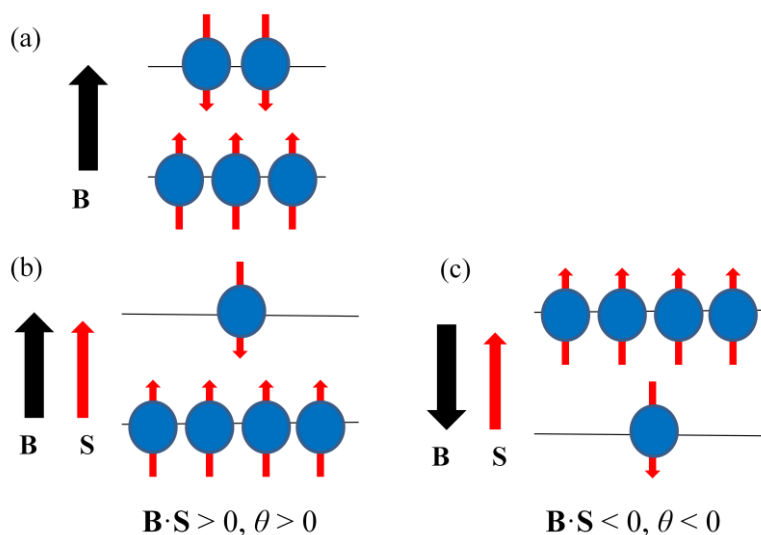


**Fig. 4.2.** Schematic images of nuclear spin distribution (a) under an external magnetic field, (b) under the DNP process when  $\mathbf{B} \cdot \mathbf{S} > 0$ , and (c) under the DNP process when  $\mathbf{B} \cdot \mathbf{S} < 0$ .

### 4.2.3 Time evolution of the nuclear spin temperature

Considering the energy balance of the nuclear spin system interacting with polarized electrons, the time ( $t$ ) evolution of nuclear spin temperature under the DNP process is described by the following equation [3]:

$$\frac{d}{dt} \left( \frac{1}{\theta} \right) = -\frac{1}{T_{1e}} \left( \frac{1}{\theta} - \frac{1}{\theta_0} \right), \quad (4.3)$$

where  $T_{1e}$  is the characteristic time for the DNP, which can be as long as 100 s or more, and  $\theta_0$  is the steady-state nuclear spin temperature, which is given by [3]

$$\frac{1}{k_B \theta_0} = f \frac{4I}{\mu_I} \frac{\mathbf{S} \cdot \mathbf{B}}{\mathbf{B}^2 + \xi B_L^2}, \quad (4.4)$$

Compare to Eq. (2.10), we know that the steady-state nuclear field is characterized by  $\theta_0$ .

### 4.2.4 Experimental conditions

In the electrical oblique Hanle effect measurements using a four-terminal non-local geometry in a lateral spin transport device (Fig. 4.3(a)), the Overhauser field can be detected through the detection of the non-local voltage  $V_{\text{NL}}$  between contacts 3 and 4. The total magnetic field of  $\mathbf{B} + \mathbf{B}_n$  induces Hanle precession for electron spins, resulting in a decrease in the electron spin polarization under detector contact-3. Similarly to the conventional Hanle signal,  $V_{\text{NL}}$  can be described by Eq. (2.6), where  $\omega_L = g\mu_B B_z / \hbar$  is the Larmor frequency, where  $B_z$  is the  $z$  component of  $\mathbf{B} + \mathbf{B}_n$ .

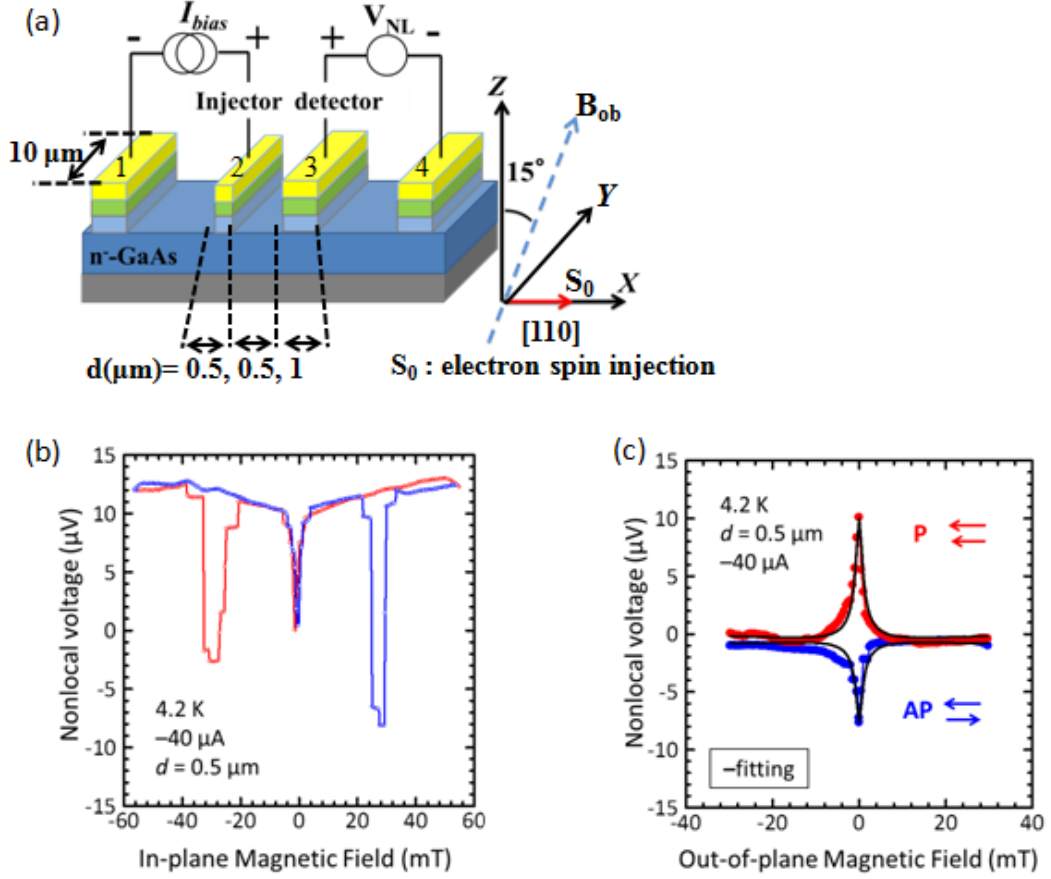


**Fig. 4.3.** (a) Schematic structure of a four-terminal non-local device and circuit configuration for oblique Hanle effect measurements. (b) Spin-valve signal and (c) Hanle signals observed in GaAs with a  $\text{Co}_2\text{MnSi}$  spin source.

To simulate a transient oblique Hanle signal, we assumed an oblique magnetic field  $\mathbf{B}_{\text{ob}}$ , which was applied along the oblique direction with  $\varphi = 15^\circ$  from the  $z$ -axis in the  $x$ - $z$  plane – *i.e.*,  $\mathbf{B}_{\text{ob}} \equiv B_{\text{ob}}(\mathbf{x}\sin\varphi + \mathbf{z}\cos\varphi)$ , where  $B_{\text{ob}}$  is the amplitude of the oblique field of  $\mathbf{B}_{\text{ob}}$  with both the positive and negative signs, and  $\mathbf{x}$  and  $\mathbf{z}$  are the unit vectors along the  $x$ -axis and  $z$ -axis directions, respectively. The device was first initiated at  $B_{\text{ob}} = +42$  mT for a hold time ( $t_{\text{hold}}$ ) of 60 s, so that nuclear spins became dynamically polarized. Then  $B_{\text{ob}}$  was swept from +42 mT to –42 mT (negative sweep direction) and was swept back from –42 mT to +42 mT (positive sweep direction) with a sweep rate of 0.18 mT/s. In addition to  $\mathbf{B}_{\text{ob}}$ , we assumed a constant stray field  $B_{\text{st}} = 0.5$  (mT) from the ferromagnetic electrodes, which pointed along the  $z$ -axis direction in the GaAs channel, as part of the external field in our simulation. Then,

the total external magnetic field  $\mathbf{B}$  was given by

$$\mathbf{B} = \mathbf{B}_{\text{ob}} + B_{st} \mathbf{z} = B_{\text{ob}}(\mathbf{x}\sin\varphi + \mathbf{z}\cos\varphi) + B_{st} \mathbf{z} , \quad (4.5)$$

where  $B_{\text{ob}}$  as a function of  $t$  is given by

$$B_{\text{ob}}(t) = \begin{cases} 42 & (0 \leq t \leq 60) \\ 42 - 0.18(t - 60) & \left(60 < t \leq 60 + \frac{84}{0.18}\right) \\ -42 + 0.18\left(t - 60 - \frac{84}{0.18}\right) & \left(60 + \frac{84}{0.18} < t \leq 60 + \frac{168}{0.18}\right) \end{cases} . \quad (4.6)$$

There are three kinds of nuclei in GaAs, that is,  $^{75}\text{As}$ ,  $^{69}\text{Ga}$ , and  $^{71}\text{Ga}$ . To distinguish the contribution of each kind of nuclei, we use three kinds of nuclear spin temperature to characterize  $^{75}\text{As}$ ,  $^{69}\text{Ga}$ , and  $^{71}\text{Ga}$  nuclei, respectively. So the total nuclear field consists of three components. From Eqs. (4.4), (4.5), and (4.6),  $\theta_0$  in Eq. (4.3) is  $t$ -dependent. Thus, we solved Eq. (4.3) numerically by dividing  $t$  into a time step of 1 s, during which  $B_{\text{ob}}$  is assumed to be constant. Substituting numerically solved  $\theta$  into Eqs. (4.2), (2.9), and (2.6), we simulated the transient response of  $\mathbf{B}_n$  and  $V_{\text{NL}}$  against a change in the magnetic field.

Parameters used in our simulation are shown in Table 4.1. The values of  $2|\mathbf{S}_0|$ ,  $l_{\text{sf}}$ , and  $\tau_{\text{sf}}$  in Table 4.1 were estimated from the fitting of our previous experimental results of the spin-valve signal ( $V_{\text{NL}}$  vs. in-plane magnetic field along the x-axis) and Hanle signals ( $V_{\text{NL}}$  vs. out-of-plane magnetic field) observed in a lateral spin transport device with  $\text{Co}_2\text{MnSi}/\text{CoFe}$  electrodes [4], where  $|\mathbf{S}_0|$  is the average electron spin at  $\mathbf{B} = \mathbf{0}$ . These results are shown in Fig. 4.3(b) and (c), respectively, and the details of the device structure and experimental conditions are described in Ref. 4. The projection of  $\mathbf{S}$  to  $\mathbf{B}$  in Eq. (4.4) was estimated from  $|\mathbf{S}_0|$ . Although the Hanle precession through  $\mathbf{B} + \mathbf{B}_n$  changes the component of  $\mathbf{S}$  perpendicular to  $\mathbf{B}$ , it does not change the component of  $\mathbf{S}$  parallel to  $\mathbf{B}$ . Thus, we assumed that  $\mathbf{S} \cdot \mathbf{B}$  is equal to  $\mathbf{S}_0 \cdot \mathbf{B}$  in the simulation. We considered three kinds of nuclei  $^{69}\text{Ga}$ ,  $^{71}\text{Ga}$ , and  $^{75}\text{As}$  in the GaAs channel. The values of  $b_n$ ,  $T_{1e}$ , and  $f$  in Table I were treated as fitting parameters. The values of  $I$  and  $\gamma$  were taken from Ref. 5, and the value of  $\sqrt{\xi} B_L$  was taken from Ref. 6.

**Table 4.1.** Summary of simulation parameters.

Parameter	Value
$2 \mathbf{S}_0 $	4.4 %
$\tau_s$	10 ns
$l_{sf}$	5 $\mu\text{m}$
$b_n$ of $^{75}\text{As}$	-4.59 T
$b_n$ of $^{69}\text{Ga}$	-2.19 T
$b_n$ of $^{71}\text{Ga}$	-1.99 T
$T_{1e}$	400 s
$f$	0.85
$I^{\text{a)}}$	3/2
$\gamma$ of $^{75}\text{As}^{\text{a)}}$	$4.581 \times 10^7$ rad/T s
$\gamma$ of $^{69}\text{Ga}^{\text{a)}}$	$6.420 \times 10^7$ rad/T s
$\gamma$ of $^{71}\text{Ga}^{\text{a)}}$	$8.158 \times 10^7$ rad/T s
$\sqrt{\xi} B_L^{\text{b)}}$	5 mT
$d$	0.5 $\mu\text{m}$
$B_{st}$	0.5 mT

a) Ref. 5. b) Ref. 6.

### 4.3 Simulation results and discussion

Figure 4.4 shows (a) a typical oblique Hanle signal observed in GaAs with a  $\text{Co}_2\text{MnSi}$  spin source [4] and (b) a corresponding simulation result [7]. Compared with the steady-state signal, we experimentally observed the following two features: (1) An additional side peak was observed at  $B_{\text{ob}} < 0$  in the negative sweep direction, and (2) no side peak was observed in the positive sweep direction, showing a clear hysteretic nature depending on the sweep direction. These features were well reproduced by using the concept of nuclear spin temperature. The value  $T_{1e} = 400$  s used in the simulation is reasonable as a time scale needed for the DNP [4, 8-9]. These results validate the simulation model used in this study. A slight deviation between the experiment and simulation for  $B_{\text{ob}} > 0$  is possibly due to the instability of the background signal during the measurement. Although we subtracted a background signal consisting of a constant term and linear and quadratic terms of  $B_{\text{ob}}$ , some uncertain background signals might be remained.

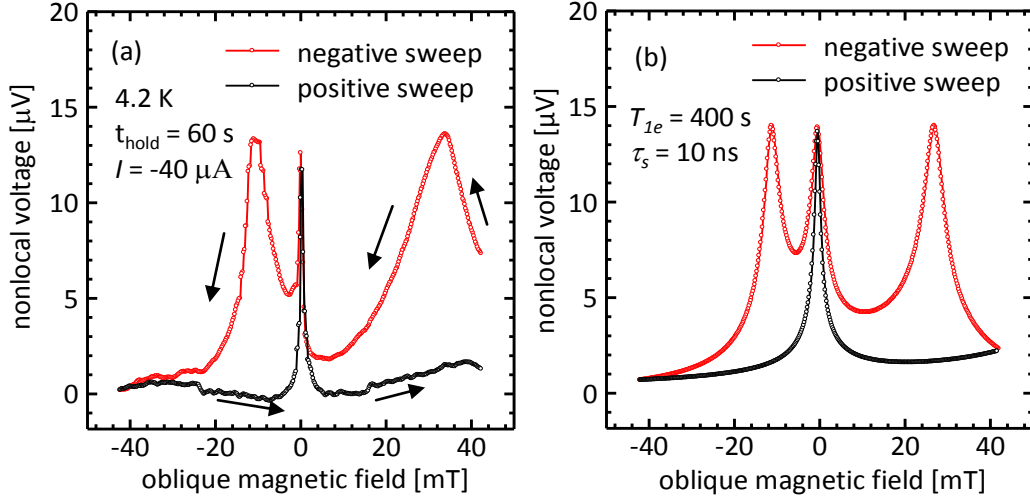


**Fig. 4.4.** (a) Oblique Hanle signal observed in GaAs with a  $\text{Co}_2\text{MnSi}$  spin source.

(b) A corresponding simulation result.

Now we will discuss the transient behavior of nuclear spins based on the time evolution of nuclear spin temperature. Because  $b_n$  is negative in GaAs, we know from Eqs. (2.7) and (4.2) that if  $\theta$  is positive (negative),  $\mathbf{I}_{av}$  is parallel (antiparallel) to  $\mathbf{B}$ , while  $\mathbf{B}_n$  is antiparallel (parallel) to  $\mathbf{B}$ . Thus, a condition that  $\mathbf{B}$  and  $\mathbf{B}_n$  cancel each other exists only for  $\theta > 0$ . Fig. 4.5 shows (a)  $B_{ob}$ ,  $B_n$  and (b)  $1/\theta$ ,  $1/\theta_0$  of  $^{75}\text{As}$  nuclei as a function of time, and (c) a simulation result of an oblique Hanle signal, and Fig. 4.6 shows corresponding nuclear spin distribution of the transient oblique Hanle effect measurement. The value of  $1/\theta$  increased during a holding time due to DNP, resulting in the nuclear field  $\mathbf{B}_n$  being generated antiparallel to  $\mathbf{B}$  at  $t = t_{hold}$  [state-1 and Fig. 4.6(a)]. When  $B_{ob}$  reached 27 mT in the negative sweep direction,  $\mathbf{B}_n$  and  $\mathbf{B}$  cancelled each other out, leading to one side peak in the non-local voltage  $V_{NL}$  [state-2 and Fig. 4.6(a)]. When  $\mathbf{B}$  was reversed,  $\theta_0$  became negative because  $\mathbf{B} \cdot \mathbf{S} < 0$ . This means that  $\mathbf{B}$  and  $\mathbf{B}_n$  should be parallel and no cancellation should occur in the steady state. However, we observed a clear side peak at  $B_{ob} = -11$  mT [state-3 and Fig. 4.6(b)], indicating cancellation between  $\mathbf{B}$  and  $\mathbf{B}_n$ . This is because  $\mathbf{B}_{ob}$  was changed before the nuclear spin system reached the steady-state. Indeed,  $1/\theta$  was delayed with respect to  $1/\theta_0$  as shown in Fig. 4.5(b), and  $\theta$  stayed positive for a certain time after  $\mathbf{B}$

was reversed. This time delay happened because the external magnetic field was changed much faster than  $T_1$  and  $T_{1e}$  processes. After  $\mathbf{B}$  was reversed, as shown in Fig. 4.6(b), the nuclear spin system adiabatically changed their spin direction to keep the Zeeman energy in the low-energy state for the negative  $B_{ob}$  as for the positive  $B_{ob}$ , resulting in a positive nuclear spin temperature. However, after sufficient time, that is, at  $t > 405$  s, a population inversion of nuclear spins occurred owing to the DNP process and  $\theta$  became negative, indicating  $\mathbf{B}_n$  was parallel to  $\mathbf{B}$  [state-4 and Fig. 4.6(c)]. Similarly in the positive sweep direction,  $\theta$  was negative ( $\mathbf{B}$  and  $\mathbf{B}_n$  were parallel) at  $B_{ob} < 0$ , and it stayed negative for a certain time after  $\mathbf{B}_{ob}$  was reversed from the negative direction to the positive direction [state-5 and Fig. 4.6(d)]. Thus, no cancellation occurred between  $\mathbf{B}$  and  $\mathbf{B}_n$ , resulting in the disappearance of the satellite peak at  $B_{ob} > 0$  for the positive sweep direction.

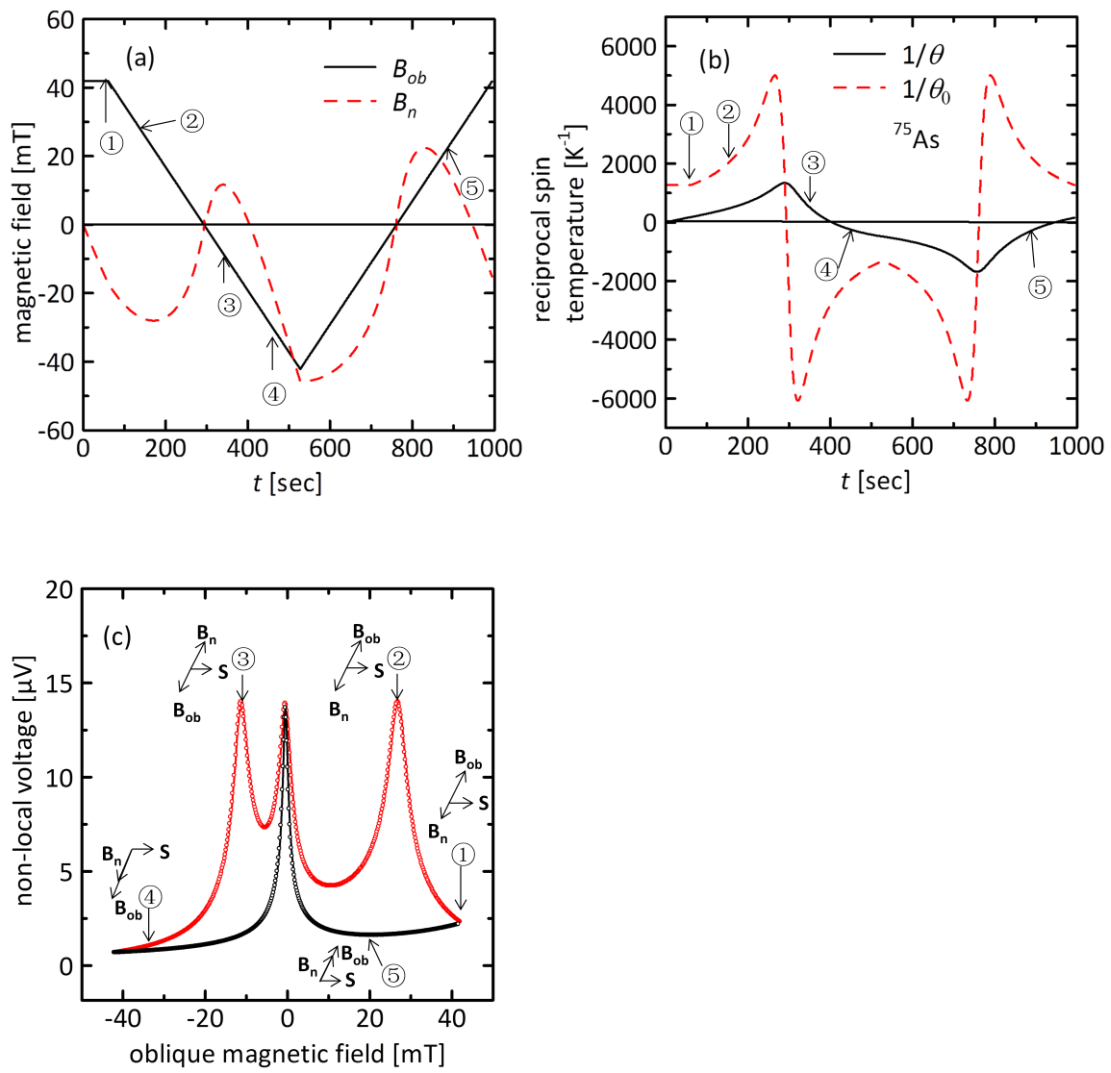


**Fig. 4.5.** (a) Time evolution of (a)  $B_{ob}$  and  $B_n$ , (b)  $1/\theta$  and  $1/\theta_0$  of  $^{75}\text{As}$  isotope in GaAs. (c) A simulation result of oblique Hanle signal.

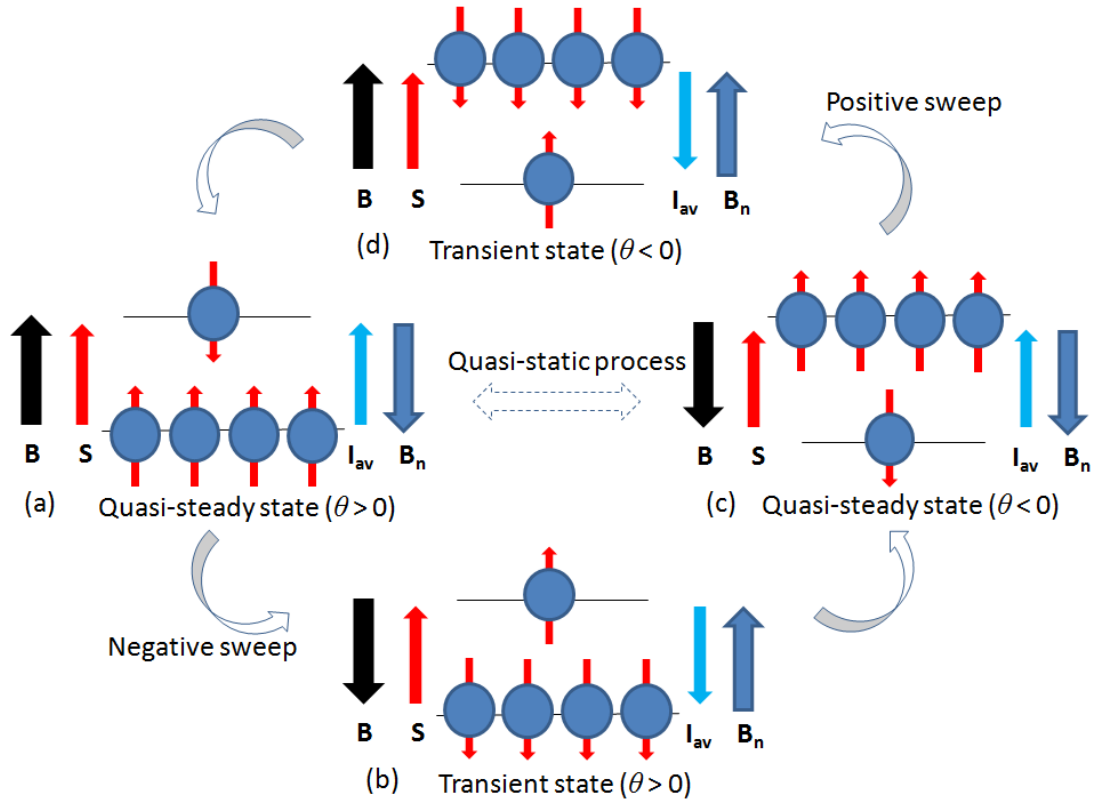


**Fig. 4.6.** Schematic images of nuclear spin distribution of the transient oblique Hanle effect measurement for (a) state-1 and state-2, (b) state-3, (c) state-4, and (d) state-5.

## 4.4 Summary

The transient response of nuclear spins in GaAs to a change in the magnetic field was analyzed by using the concept of nuclear spin temperature. The hysteretic nature of nuclear field with respect to the sweep direction of the external magnetic field, which originated from the transient response of nuclear spins, was well reproduced by this method. From the analysis, we found that this behavior can be understood by the delay of the time response of nuclear spin temperature to a change in the magnetic field. Also, the simulation provides one method to estimate the time scale of the DNP.

## References

- [1] A. Abragam and W. G. Proctor, Phys. Rev. **109**, 1441 (1958).
- [2] A. Abragam, in *The Principles of Nuclear Magnetism* (Oxford University Press, Oxford, 1961), Chap. I.
- [3] M. I. Dyakonov and V. I. Perel, in *Optical Orientation*, ed. F. Meier and B. P. Zakharchenya (North-Holland, Amsterdam, 1984), Chap. 2.
- [4] T. Akiho, J. Shan, H. -x. Liu, K. -i. Matsuda, M. Yamamoto, and T. Uemura, Phys. Rev. B. **87**, 235205 (2013).
- [5] D. Paget and V. L. Berkovits, in *Optical Orientation*, ed. F. Meier and B. P. Zakharchenya (North-Holland, Amsterdam, 1984), Chap. 9.
- [6] M. K. Chan, Q. O. Hu, J. Zhang, T. Kondo, C. J. Palmstrøm, and P. A. Crowell, Phys. Rev. B **80**, 161206(R) (2009).
- [7] Z. Lin, K. Kondo, M. Yamamoto, and T. Uemura, Jpn. J. Appl. Phys. **55**, 04EN03 (2016).
- [8] J. Strand, X. Lou, C. Adelman, B. D. Schultz, A. F. Isakovic, C. J. Palmstrøm, and P. A. Crowell, Phys. Rev. B **72**, 155308 (2005).
- [9] P. Van Dorpe, W. Van Roy, J. De Boeck, and G. Borghs, Phys. Rev. B **72**, 035315 (2005).



# 5. Detection of nuclear spin coherence through spin-echo measurements

## 5.1 Introduction

Nuclear spins are promising implementations for qubits because they have extremely long coherence times. The nuclear magnetic resonance (NMR) technique enables the control and detection of nuclear-spin-based qubits. However, the sensitivity of the conventional NMR technique is limited by the low magnetic moments of the nuclear spins, which are three orders of magnitude smaller than that of the electron spins. Dynamic nuclear polarization (DNP), where nuclear spins are dynamically polarized through a hyperfine interaction between nuclear spins and electron spins, has attracted much interest, since it can dramatically increase the NMR signal. To generalize electron spins, methods such as optical polarization, quantum Hall system, and spin injection are used. Coherent manipulation of nuclear spins in semiconductors by NMR with DNP has been demonstrated electrically in GaAs/AlGaAs quantum Hall systems by observing the Rabi oscillation [1-3] and optically in GaAs/AlGaAs quantum wells by observing the Rabi oscillation and spin-echo signals [4]. Although the optical method is suitable for clarifying the fundamental physics of nuclear spins, it is restricted in its scalability because the spatial resolution is limited by the optical wavelength. The quantum Hall systems require a strong magnetic field of several Tesla and a low temperature below 1 K to create highly polarized electron spins for DNP. Considering these shortcomings, a spin injection system is a better choice since it is all electrical and a highly polarized spin source allows efficient DNP without a strong magnetic field.

Recently, we developed a novel NMR system that uses spin injection from a highly polarized spin source and detected the Rabi oscillation electrically with a static magnetic field of  $\sim 0.1$  T at 4.2 K [5]. A Mn-rich  $\text{Co}_2\text{MnSi}$  was used as a spin source and we have demonstrated high-efficiency spin injection from  $\text{Co}_2\text{MnSi}$  into

GaAs via an ultrathin insertion layer of CoFe in a spin injection device, resulting in a high electron spin polarization as described in Chap. 3. This enabled efficient DNP and sensitive detection of the Rabi oscillation even at a low magnetic field and a relatively high temperature [5].

For achieving nuclear-spin-based qubits, it is important to clarify the nuclear-spin phase coherence time  $T_2$ , because the lifetime of a qubit is limited by  $T_2$ . In a real system, however, the decoherence is enhanced due to the inhomogeneity in the external magnetic field. The real coherence time  $T_2^*$  can be estimated from the Rabi oscillation as  $T_2^* = 1/2T_2^{\text{Rabi}}$ , and it consists of an intrinsic component  $T_2 = 1/\gamma B_L$ , which results from the dipolar-dipolar interaction between the nuclear spins, and the other component  $T_2^{\text{inhom}} = 1/\gamma \Delta B_{\text{ext}}$ , which results from the inhomogeneity in the external magnetic field.  $T_2$  is the intrinsic coherence time and it is determined by the material itself while  $T_2^{\text{inhom}}$  is extrinsic and determined by the measurement system. In order to know the intrinsic  $T_2$ , a spin echo measurement [4, 6], which refocuses nuclear-spin magnetization by using a specific pulse sequence, has to be made to exclude the  $T_2^{\text{inhom}}$  component.

The purpose of the present study is to clarify the phase coherence time  $T_2$  of the nuclear spins in GaAs through an electrical spin-echo measurement in a spin injection device. Since the durations of  $\pi/2$  and  $\pi$  pulses should be determined when performing a spin-echo measurement, the Rabi oscillation was also measured, as was done in our previous work [5].

## 5.2 Experimental methods and results

### 5.2.1 Device structure

A lateral spin transport device having  $\text{Co}_2\text{MnSi}/\text{CoFe}$  (1.3 nm)/GaAs heterojunctions was fabricated (Fig. 5.1). The layer structure and device geometry are described in section 3.2. The device operation includes: (1) Generation of spin-polarized electrons in GaAs by spin injection; (2) Initialization of nuclear spins

by DNP; (3) Quantum manipulation of nuclear spins through the NMR effect; (4) Readout of nuclear spin states through the detection of the non-local voltage ( $V_{NL}$ ) between electrode-3 and electrode-4. The non-local voltage is a measure of the response of the electron spins to the total magnetic field of both the nuclear field and external magnetic field. Through the NMR effect, the nuclear spins, or the nuclear field, are manipulated, resulting in the changes in the non-local voltage. Thus, the nuclear spin states can be read out from the changes of the non-local voltage ( $\Delta V_{NL}$ ). The creation, control, and detection of the nuclear spins in GaAs were evaluated in a four-terminal non-local geometry when  $V_{NL}$  between electrode-3 and electrode-4 was measured under a constant current  $I$  supplied between electrode-2 and electrode-1 under a static magnetic field  $\mathbf{B}_0$  and an RF magnetic field  $\mathbf{B}_{rf}$ . The  $\mathbf{B}_{rf}$  was generated by an 11-turn coil with a diameter of 1.0 cm for the NMR experiment. All the measurements were done at 4.2 K.

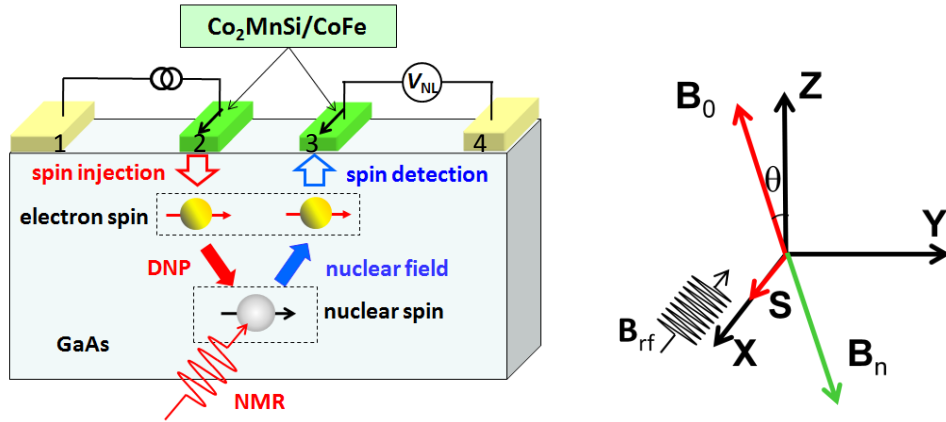


**Fig. 5.1.** Experimental setup of NMR for a lateral spin transport device. The injected electron spins are along the  $x$ -axis. Taking  $\mathbf{B}_0 \cdot \mathbf{S} > 0$  and  $b_n < 0$  in Eq. (2.10) into consideration,  $\mathbf{B}_n$  is anti-parallel to  $\mathbf{B}_0$ .

We observed clear spin-valve signals (Fig. 5.2(a)) and Hanle signals (Fig. 5.2(b)), which are evidence of successful spin injection from this device [7]. The estimated values of  $\tau_s$ ,  $l_{sf}$ , and the effective spin polarization defined by  $|P_{inj}P_{det}|^{1/2}$  in Eq. (2.6) were  $\tau_s = 20$  ns,  $l_{sf} = 3$   $\mu\text{m}$ , and  $|P_{inj}P_{det}|^{1/2} = \sim 30\%$ , respectively.

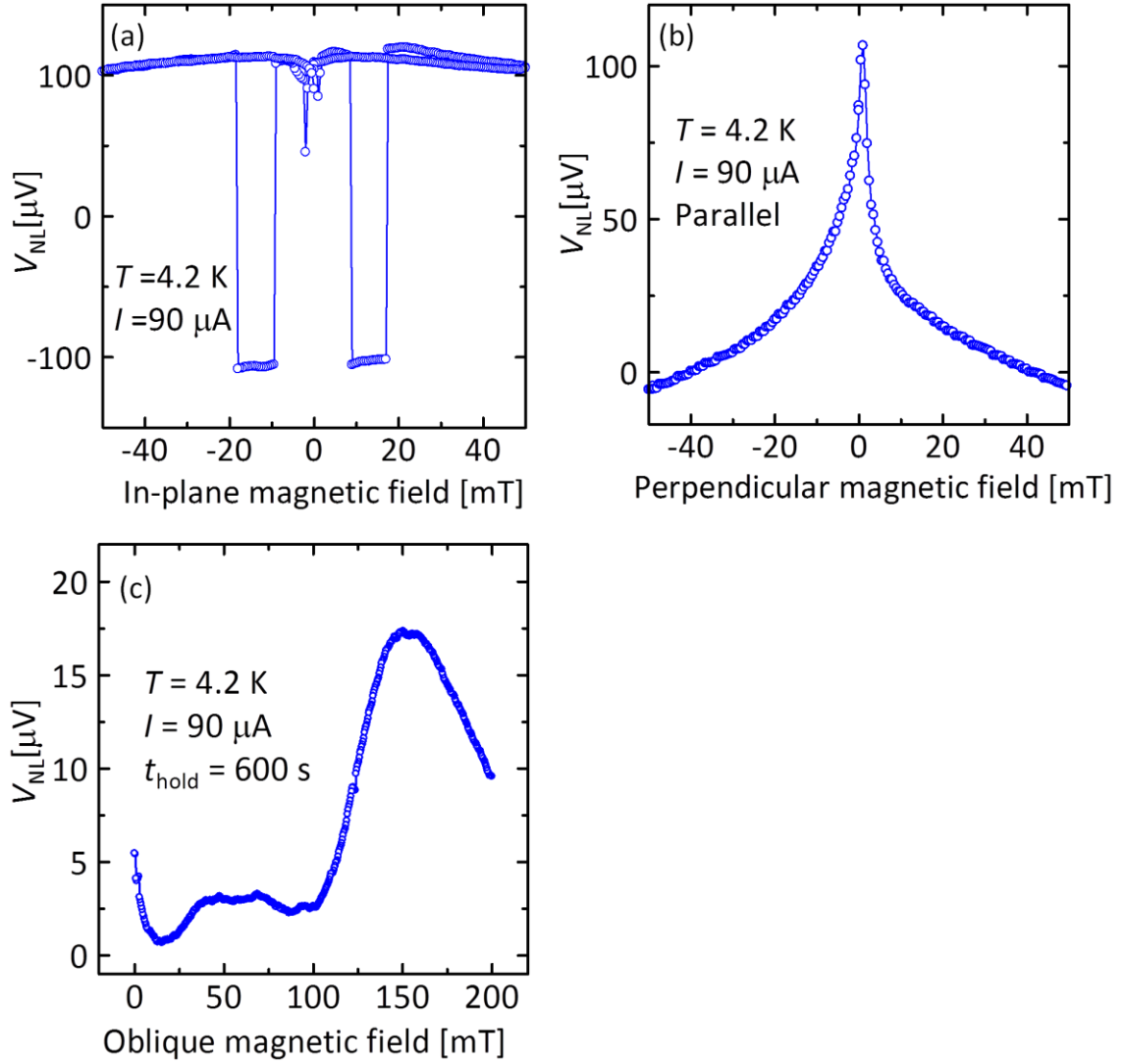


**Fig. 5.2.** (a) Spin-valve signals, (b) Hanle signals and (c) Oblique Hanle signals measured at 4.2 K with a constant current  $I = 90$   $\mu\text{A}$ .

## 5.2.2 Initialization of DNP

This high spin polarization in GaAs due to the spin injection from a highly polarized spin source of Co<sub>2</sub>MnSi is promising for DNP. In order to check whether the DNP occurs in our device, the oblique Hanle signal (Fig. 5.2(c)) was measured. The magnetic field  $\mathbf{B}_0$  ( $|\mathbf{B}_0| = 200$  mT) was applied to the device along a direction a small angle  $\theta \approx 8^\circ$  from the  $z$ -axis in the  $x$ - $z$  plane for a holding time  $t_{\text{hold}} = 600$  s, and then it was swept from 200 mT to 0 with a sweep rate of 0.4 mT/s. From Eq. (2.10),  $\mathbf{B}_n$  and  $\mathbf{B}_0$  are parallel or antiparallel, depending on the sign of  $b_n \mathbf{B}_0 \cdot \mathbf{S}$ . When  $\mathbf{B}_0 = \mathbf{0}$ ,  $\mathbf{S}$  points along the  $x$ -axis, whereas when  $\mathbf{B}_0 \neq \mathbf{0}$ ,  $\mathbf{S}$  precesses along  $\mathbf{B}_0 + \mathbf{B}_n$ . This precession changes only the component of  $\mathbf{S}$  perpendicular to  $\mathbf{B}_0$ , and conserves the component of  $\mathbf{S}$  parallel to  $\mathbf{B}_0$ , resulting in  $\mathbf{B}_0 \cdot \mathbf{S} > 0$  in this magnetic field configuration. Taking  $b_n < 0$  in Eq. (2.10) into consideration,  $\mathbf{B}_n$  is generated along the direction antiparallel to  $\mathbf{B}_0$ . The  $V_{\text{NL}}$  plotted in Fig. 5.2(c) can be described by Eq. (2.6) by replacing  $\mathbf{B}_0$  with  $\mathbf{B}_0 + \mathbf{B}_n$ . When  $|\mathbf{B}_0|$  was swept from +200 mT to 0,  $|\mathbf{B}_0 + \mathbf{B}_n|$  reached a local minimum at  $|\mathbf{B}_0| = 150$  mT, resulting in  $V_{\text{NL}}$  having a side peak at  $|\mathbf{B}_0| = 150$  mT. In other words, the observation of the side peak is a clear indication of DNP.

For the NMR measurements including the Rabi oscillation measurement and the spin-echo measurement, the nuclear spins should be initialized by the DNP. For initialization, a static magnetic field  $\mathbf{B}_0$  with a strength of  $|\mathbf{B}_0| = 114$  mT was applied to the device along the direction by a small angle  $\theta \approx 8^\circ$  from the  $z$ -axis in the  $x$ - $z$  plane for approximately 10 minutes (Fig. 5.1). Similarly to the oblique Hanle signal measurement shown in Fig. 5.2(c), the electron spins injected from the Co<sub>2</sub>MnSi spin source should polarize the nuclear spins through the DNP process, resulting in a nuclear field  $\mathbf{B}_n$  being anti-parallel to  $\mathbf{B}_0$ .

### 5.2.3 Resonance condition for $^{69}\text{Ga}$ nuclear spins

To determine the resonance frequency for the NMR measurements, an RF magnetic field  $\mathbf{B}_{\text{rf}}$  was continuously applied to the device along the  $x$ -axis (Fig. 5.1). The frequency of the RF magnetic field was swept up or down with a rate of 200 Hz/s. As shown in Fig. 5.3, when the frequency was swept to approximately 1.118 MHz, an obvious change occurred in the non-local voltage. This is because the nuclear spins became depolarized when the NMR occurred. As described in Chap. 2, the non-local voltage is a measure of the response of the electron spin precession along the effective magnetic field of  $\mathbf{B}_0 + \mathbf{B}_n$ . The depolarization of the nuclear spins led to a decrease in  $\mathbf{B}_n$ , resulting in a change in the electron spin precession. The non-local voltage increased because the total magnetic field was decreased and consequently, the electron spin precession was suppressed. This resonance frequency was close to the theoretical value of  $^{69}\text{Ga}$  nuclear spins given by Eq. (2.2) under a magnetic field of 114 mT. Therefore, the resonance frequency for  $^{69}\text{Ga}$  nuclear spins is determined to be 1.118 MHz, and in the following, NMR measurements will be conducted on  $^{69}\text{Ga}$  nuclear spins.

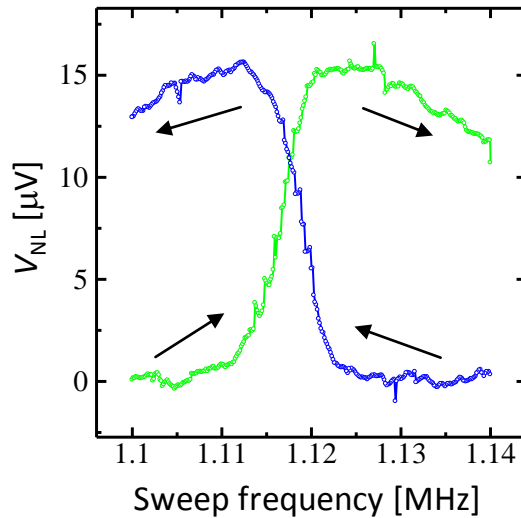


**Fig. 5.3.** Frequency dependence of the non-local voltage under a static magnetic field of 114 mT. The RF magnetic field was continuously applied and frequency was swept up or down with a rate of 200 Hz/s.

## 5.2.4 Rabi oscillation of $^{69}\text{Ga}$ nuclear spins

To determine the durations for  $\pi/2$  and  $\pi$  pulses which are needed for the spin-echo measurement, the Rabi oscillation of the nuclear spins should be measured. In the following, the experimental result of the Rabi oscillation of  $^{69}\text{Ga}$  nuclear spins will be introduced.

After the initialization of the nuclear spins, an RF magnetic field  $\mathbf{B}_{\text{rf}}$  was applied along the  $x$ -axis with a certain pulse duration  $\tau_p$  and a frequency of 1.118 MHz, corresponding to the resonance frequency of  $^{69}\text{Ga}$  in a static magnetic field  $|\mathbf{B}_0| = 114$  mT. Then, the nuclear spins of  $^{69}\text{Ga}$  were rotated by an angle of  $\gamma(^{69}\text{Ga})|\mathbf{B}_{\text{rf}(m)}|\tau_p/2$  in the rotating frame which rotates along the  $z$ -axis with a rotating frequency synchronized to the resonance frequency of  $^{69}\text{Ga}$ , where  $\gamma(^{69}\text{Ga})$  is the gyromagnetic ratio of  $^{69}\text{Ga}$  and  $|\mathbf{B}_{\text{rf}(m)}|$  is the amplitude of  $\mathbf{B}_{\text{rf}}$ . Consequently, the  $^{69}\text{Ga}$  component of  $\mathbf{B}_n$  was rotated, and the total magnetic field was changed, resulting in a change in  $V_{\text{NL}}$  according to Eq. (2.6). Figure 5.4(a) shows the time evolution of  $V_{\text{NL}}$  when  $\mathbf{B}_{\text{rf}}$  pulses with  $\tau_p = 30, 50$  and  $70 \mu\text{s}$  were applied at  $t = 0$ .  $V_{\text{NL}}$  increased rapidly by  $\Delta V_{\text{NL}} = 7, 13$  and  $16 \mu\text{V}$ , respectively, and then it gradually recovered to its initial state on a time scale of several hundreds of seconds [7]. The increase in  $V_{\text{NL}}$  due to the irradiation of the RF pulse indicates that the Hanle precession became weaker as a result of the decrease in the  $z$  component of the effective magnetic field,  $B_z$ . The value of  $B_z$  after the irradiation of a pulse with a duration of  $\tau_p$  is given by

$$B_z(\tau_p) = A_1 \cos(2\pi f_{\text{Rabi}} \tau_p) \exp(-\tau_p / T_2^{\text{Rabi}}) - A_2, \quad (5.1)$$

where  $A_1$  and  $A_2$  are constants,  $f_{\text{Rabi}} (= \gamma(^{69}\text{Ga})|\mathbf{B}_{\text{rf}(m)}|/4\pi)$  is the frequency for the oscillation of  $B_z$ , and  $T_2^{\text{Rabi}}$  is the effective dephasing time. We define  $\Delta V_{\text{NL}}$  as the change in  $V_{\text{NL}}$  just after the  $\mathbf{B}_{\text{rf}}$  pulse. The oscillatory behavior of  $B_z$  induces an oscillation in  $\Delta V_{\text{NL}}$  as a function of  $\tau_p$ . Figure 5.4(b) shows the  $\tau_p$  dependence of  $\Delta V_{\text{NL}}$ , along with a fitting curve calculated by substituting Eq. (5.1) into Eq. (2.6) [7]. We observed clear oscillations in  $\Delta V_{\text{NL}}$  as a function of  $\tau_p$ . From the fitting,  $T_2^{\text{Rabi}} = 320 \mu\text{s}$  and  $f_{\text{Rabi}} = 5.4 \text{ kHz}$  were obtained, from which the amplitude of  $\mathbf{B}_{\text{rf}}$  was estimated

to be  $\sim 1$  mT. The value of  $T_2^{\text{Rabi}} = 320 \mu\text{s}$  was smaller than that of  $400 \mu\text{s}$  previously reported in Ref. [5]. This difference mainly owes to the enhancement of the dipole-dipole interactions accompanying a slight increase in  $\theta$  from  $5^\circ$  to  $8^\circ$  degrees, as was discussed in Ref. [4]. From the period of the Rabi oscillation, the durations for  $\pi/2$  and  $\pi$  pulses were determined to be  $46$  and  $92 \mu\text{s}$ , respectively.

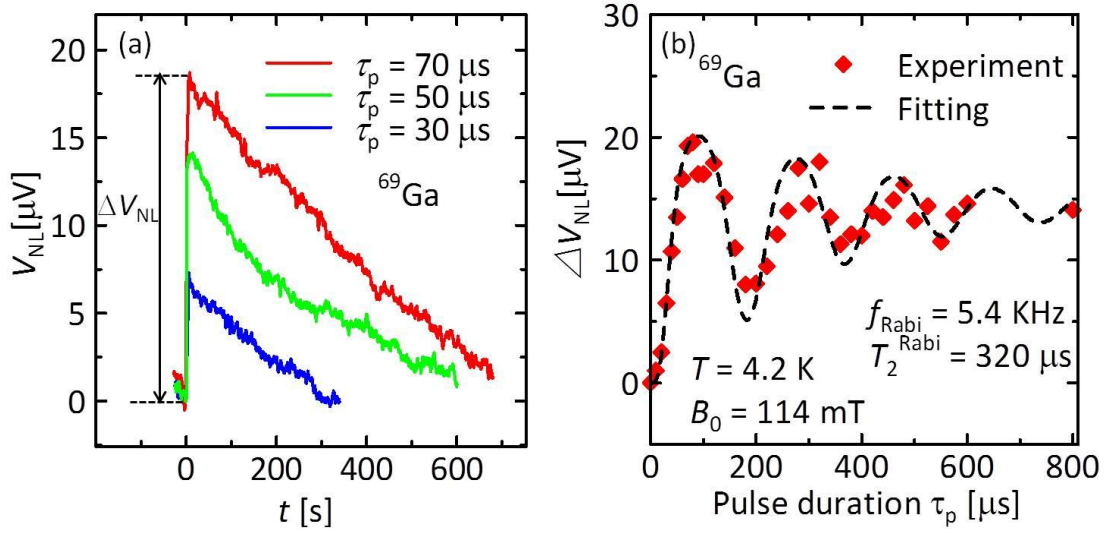


**Fig. 5.4.** (a) Time evolution of  $V_{\text{NL}}$  when  $\mathbf{B}_{\text{rf}}$  pulses with  $\tau_p = 30, 50$  and  $70 \mu\text{s}$  were applied at  $t = 0$ .  $V_{\text{NL}}$  was offset by  $10.9 \text{ mV}$ , so that  $V_{\text{NL}} = 0$  at  $t = 0$ . (b)  $\tau_p$  dependence of  $\Delta V_{\text{NL}}$  along with a fitting curve, where  $\Delta V_{\text{NL}}$  is defined as the change in  $V_{\text{NL}}$  just after the  $\mathbf{B}_{\text{rf}}$  pulse.

### 5.2.5 Spin echo signal of $^{69}\text{Ga}$ nuclear spins

Finally, the spin echo signal of  $^{69}\text{Ga}$  nuclear spins will be introduced. In the spin echo measurement, a pulse sequence consisting of  $\pi/2$ ,  $\pi$ , and  $\pi/2$  pulses (Fig. 5.5) is applied to nuclear spins that are initialized to be along the  $z$ -axis (Fig. 5.5(a)). The first  $\pi/2$  pulse rotates the nuclear spins by  $\theta = \pi/2$  to the  $y$ -axis in the rotating frame (Fig. 5.5(b)), and the nuclear spins start to dephase due to the inhomogeneous external magnetic field. After a time of  $\tau/2$ , the nuclear spins split because each nuclear spin rotates with a different speed (Fig. 5.5(c)). Some nuclear spin rotates fast and the rotation angle from the  $y$ -axis is larger, and some nuclear spin rotates slowly and the rotation angle from the  $y$ -axis is smaller. At this time, if we apply a  $\pi$  pulse, then the nuclear spins are rotated along the  $x$ -axis by  $\theta = \pi/2$  and they start to refocus (Fig. 5.5(d)), which is just the reversal process of the dephasing in Fig. 5.5(c). After the same time of  $\tau/2$ , the nuclear spins will rotate to the minus  $y$ -axis with an angle equal to that they just rotated from the  $y$ -axis. Then a complete refocusing, or spin echo, occurs (Fig. 5.5(e)). The refocusing can occur because the dephasing due to the inhomogeneous external magnetic field is reversible. Finally, the second  $\pi/2$  pulse rotates the nuclear spins back to the  $z$ -axis for readout (Fig. 5.5(f)). After the application of the pulse, the nuclear field decays due to the local field  $\mathbf{B}_L$ , resulting in a change in the effective magnetic field, which can be detected by the non-local voltage  $V_{\text{NL}}$ .

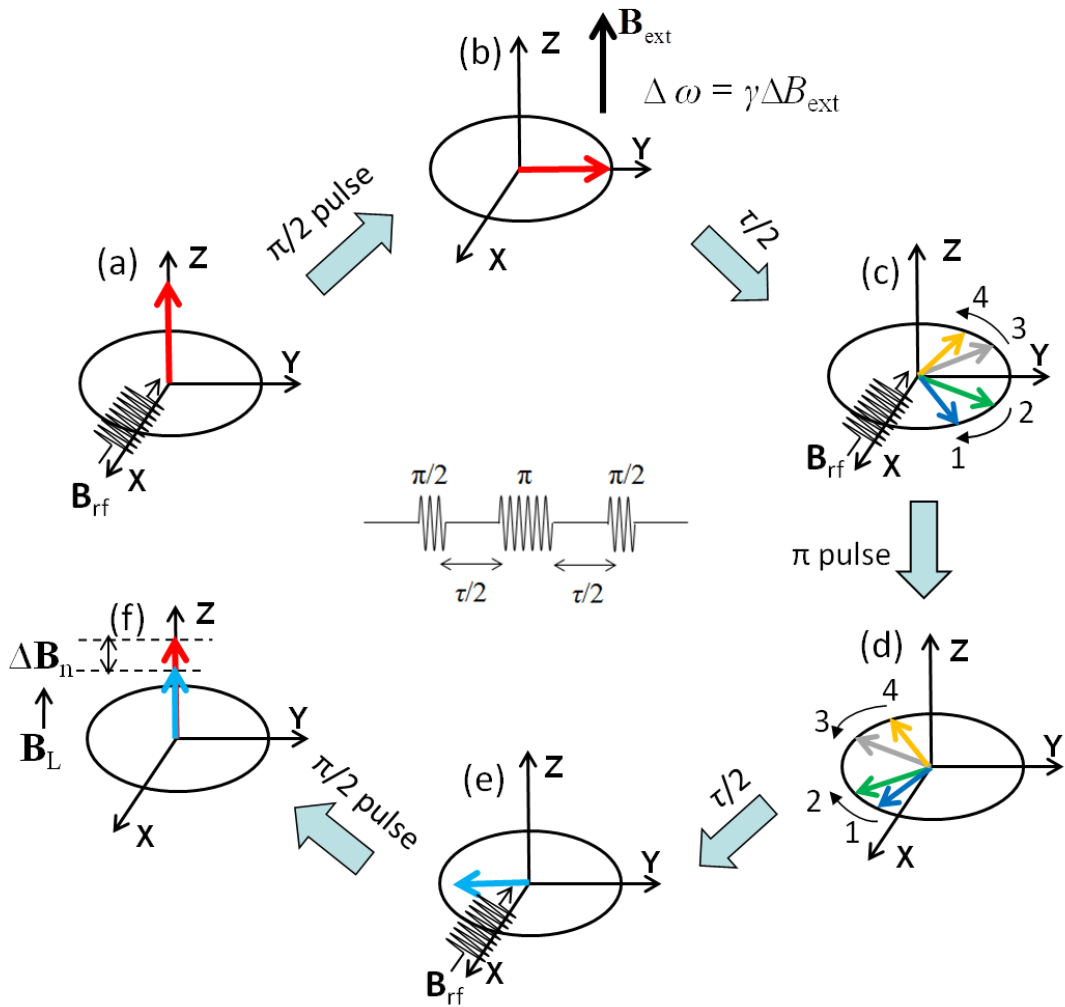


**Fig. 5.5.** Illustration of a spin-echo measurement in a rotating frame with a pulse sequence consisting of  $\pi/2$ ,  $\pi$ , and  $\pi/2$  pulses. The effective RF magnetic field is along the x-axis.

Figure 5.6(a) shows the time evolution of  $V_{\text{NL}}$  when spin-echo pulse sequences with  $\tau = 60$  and  $200 \mu\text{s}$  were applied at  $t = 0$ .  $V_{\text{NL}}$  changed rapidly by  $\Delta V_{\text{NL}} = 8.5$  and  $16 \mu\text{V}$ , respectively, after applying the pulse sequences; then it gradually recovered to its initial state [7].  $V_{\text{NL}}$  increased because the decay of  $^{69}\text{Ga}$  nuclear spins resulted in a decrease in the  $z$  component of the effective magnetic field, which is given by

$$B_z(\tau) = A_3 \exp(-\tau/T_2) - A_4, \quad (5.2)$$

where  $A_3$  and  $A_4$  are constants. Figure 5.6(b) shows the  $\tau$  dependence of  $\Delta V_{\text{NL}}$ , along with a fitting curve calculated by substituting Eq. (5.2) into Eq. (2.6) [7]. An exponential-like behavior of  $\Delta V_{\text{NL}}$ , corresponding to the intrinsic decoherence of  $^{69}\text{Ga}$  nuclear spins, was observed. The intrinsic coherence time  $T_2$  ( $= 180 \mu\text{s}$ ) was obtained from the fitting results and is comparable with the values reported in Ref. [4].

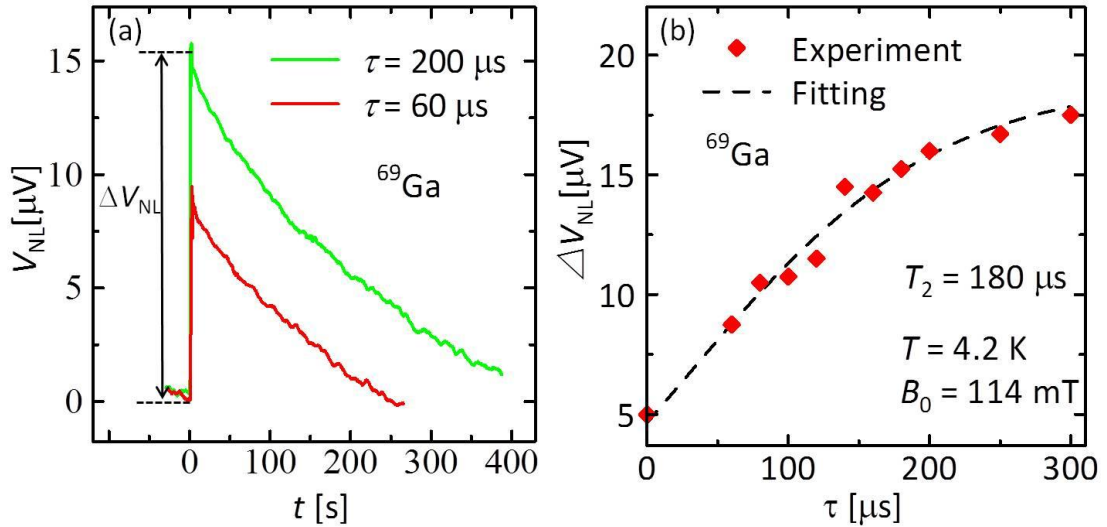


**Fig. 5.6.** (a) Time evolution of  $V_{\text{NL}}$  after applying spin-echo pulse sequence with  $\tau = 60$  and  $200 \mu\text{s}$  at  $t = 0$ .  $V_{\text{NL}}$  was offset by  $10.9 \text{ mV}$ , so that  $V_{\text{NL}} = 0$  at  $t = 0$ . (b)  $\tau$  dependence of  $\Delta V_{\text{NL}}$ . The offset of  $5 \mu\text{V}$  at  $\tau = 0$  results from the decay of the Rabi oscillation for one cycle.

### 5.3 Discussion

The real coherence time  $T_2^*$  can be estimated as  $T_2^* = 1/2T_2^{\text{Rabi}}$ . Since  $T_2^{\text{Rabi}} = 320 \mu\text{s}$ , then  $T_2^*$  should be  $160 \mu\text{s}$ . It is close to the intrinsic coherence time  $T_2 (= 180 \mu\text{s})$ , which indicates that the inhomogeneity in the external magnetic fields is not obvious. However, there is still a small difference between  $T_2^*$  and  $T_2$ , which results from the inhomogeneous external magnetic fields. In our device, the external fields consist of a static magnetic field and a stray field from the ferromagnet. Since NMR was observed within a small volume, the inhomogeneity in the static magnetic field is probably negligible. Therefore, the inhomogeneity probably comes from the stray field.

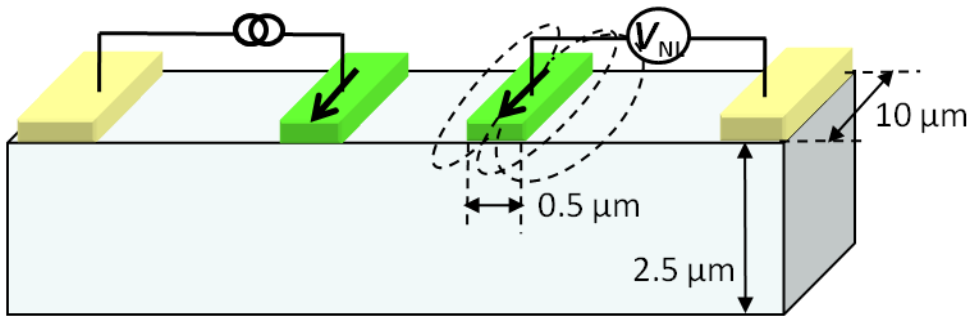


**Fig. 5.7.** Illustration of a stray field from the ferromagnet, and an electron field generated by the electron spins in the spin injection device.

## 5.4 Summary

In summary, we demonstrated spin echoes of nuclear spins in a spin injection device with a highly polarized spin source by nuclear magnetic resonance (NMR). Table 5.1 shows the position of this study among GaAs-based materials. The quantum Hall system requires a strong magnetic field and a very low temperature. The optical method is restricted in the scalability. In this study, we demonstrated the detection of nuclear spin coherence in GaAs using electrical spin injection. Efficient spin injection into GaAs from a half-metallic spin source of  $\text{Co}_2\text{MnSi}$  enabled efficient dynamic nuclear polarization (DNP) and sensitive detection of NMR signals even at a low magnetic field of  $\sim 0.1$  T and a relatively high temperature of 4.2 K. It was found that the intrinsic coherence time  $T_2$  obtained from the spin-echo signals was slightly larger than  $T_2^*$  obtained by the Rabi oscillation, which indicates that the inhomogeneity in the external fields exists. The inhomogeneity probably comes from the stray field. This study provides an all-electrical NMR system for nuclear-spin-based qubits.

**Table 5.1.** Position of this study

Material	Scalability	Temperature & Magnetic field	Nuclear spin manipulation	
			Rabi oscillation	Spin echo
AlGaAs/GaAs 2DEG[1] (Quantum Hall system)	○	T = 50 mK, B = 7.3 T	○	?
AlGaAs/GaAs QW[4] (Optical polarization)	×	T = 5.5 K, B = 0.63 T	○	○
<b>GaAs</b> <b>(Spin injection)</b>	○	T = 4.2 K, B $\cong$ 0.1 T	○	<b>This study</b>

## References

- [1] T. Machida, T. Yamazaki, K. Ikushima, and S. Komiyama, *Appl. Phys. Lett.* **82**, 409 (2003).
- [2] G. Yusa, K. Muraki, K. Takashina, K. Hashimoto, and Y. Hirayama, *Nature (London)* **434**, 1001 (2005).
- [3] H. Takahashi, M. Kawamura, S. Masubuchi, K. Hamaya, T. Machida, Y. Hashimoto, and S. Katsumoto, *Appl. Phys. Lett.* **91**, 092120 (2007).
- [4] H. Sanada, Y. Kondo, S. Matsuzaka, K. Morita, C.Y. Hu, Y. Ohno, and H. Ohno, *Phys. Rev. Lett.* **96**, 067602 (2006).
- [5] T. Uemura, T. Akiho, Y. Ebina, and M. Yamamoto, *Phys. Rev. B* **91**, 140410(R) (2015).
- [6] A. Abragam, *The Principles of Nuclear Magnetism* (Clarendon, Oxford, 1961).
- [7] Z. Lin, M. Rasly, and T. Uemura, *Appl. Phys. Lett.* **110**, 232404 (2017).

## 6. Conclusion

This research presents significant results on two aspects:

### 1. Spin injection into semiconductors

Electrical spin injection was demonstrated into bulk GaAs and AlGaAs/GaAs heterostructures using  $\text{Co}_2\text{MnSi}$  as a spin source. In bulk GaAs, a clear spin-valve signal and a Hanle signal were observed. The highly polarized spin source of  $\text{Co}_2\text{MnSi}$  leads to a high spin polarization, which is promising for the DNP process. Moreover, a clear transient oblique Hanle signal was observed in GaAs, which was evidence of nuclear spin polarization. In the AlGaAs/GaAs heterostructure, a spin-valve signal was observed up to room temperature. The spin-valve signal regarding the temperature shows relatively complicated behavior compared with that of the bulk device, which results from the opposite tendency of sheet resistance. Moreover, the spin-valve signal in the 2DEG device is less sensitive to temperature than that in the bulk device. This result contributes to a better understanding of spin transport in a 2DEG channel, which is indispensable for realizing future spin transistors that can operate at room temperature.

### 2. Nuclear spin manipulation in semiconductors

The transient response of nuclear spins in GaAs to a change in the magnetic field was analyzed by using the concept of nuclear spin temperature. The hysteretic nature of nuclear field with respect to the sweep direction of the external magnetic field, which originated from the transient response of nuclear spins, was well reproduced by this method. From the analysis, we found that this behavior can be understood by the delay of the time response of nuclear spin temperature to a change in the magnetic field. Also, the simulation provides one method to estimate the time scale of the DNP.

More importantly, we demonstrated spin echoes of nuclear spins in a spin injection device with a highly polarized spin source by nuclear magnetic resonance (NMR). Efficient spin injection into GaAs from a half-metallic spin source of

Co<sub>2</sub>MnSi enabled efficient dynamic nuclear polarization (DNP) and sensitive detection of NMR signals even at a low magnetic field of ~0.1 T and a relatively high temperature of 4.2 K. It was found that the intrinsic coherence time  $T_2$  obtained from the spin-echo signals was slightly larger than  $T_2^*$  obtained by the Rabi oscillation, which indicates that the inhomogeneity in the external fields exists. The inhomogeneity probably comes from the stray field or the electron field. This study provides an all-electrical NMR system for nuclear-spin-based qubits.

In conclusion, all the results described above attribute to the development of a spin-injection combined NMR technique for nuclear spin manipulation.

# Acknowledgements

I would like to thank my supervisor, Professor Tetsuya Uemura, for his supervision, discussion, and supports throughout this work since my master's course. Without his help, I couldn't get these achievements. Besides the research, I would also like to thank him for supporting me for scholarship application and job hunting.

I am also very grateful to thank Professor Masafumi Yamamoto for his supervision and valuable discussion during my master's course. His questions and comments helped me better understand this research.

I would also like to thank Professor Akihiro Murayama, Professor Kazuhisa Sueoka, and Professor Akihisa Tomita for their reviewing and discussion for my doctoral thesis.

I want to thank Dr. Mahmoud Rasly for his contributions to this research, especially the MBE growth and the NMR measurements. I also appreciate Mr. Da Pan for his contributions in the measurements. I would like to thank all other students of the Laboratory of Nanoscale Electron Devices for their supports, directly or indirectly to this research.

I also want to thank Mitsubishi Corporation for offering me scholarship, which is very helpful for my daily life and study.

Finally, I would like to thank my family for their supports and encouragements.



# Appendix

## 1. 論文(学位論文関係)

### I 査読付学会誌等

- (1) Z. Lin, K. Kondo, M. Yamamoto, and T. Uemura: “Transient analysis of oblique Hanle signals observed in GaAs”, Jpn. J. Appl. Phys. Vol. 55, No. 4S, 04EN03 (5pp) (2016) (IF=1.452, TC=3)
- (2) Z. Lin, M. Rasly, and T. Uemura: “Electrical detection of nuclear spin-echo signals in an electron spin injection system”, Appl. Phys. Lett. Vol. 110, No. 23, 232404 (4pp) (2017) (IF=3.495, TC=2)
- (3) Z. Lin, D. Pan, M. Rasly, and T. Uemura: “Electrical spin injection into AlGaAs/GaAs-based two-dimensional electron gas systems with Co<sub>2</sub>MnSi spin source up to room temperature”, Appl. Phys. Lett. Vol. 114, No. 1, 012405 (5pp) (2019) (IF=3.495, TC=0).

### II 査読付国際会議プロシーディング

- (1) Z. Lin, M. Yamamoto and T. Uemura: “Transient Analysis of Oblique Hanle Signals Observed in GaAs”, 2015 International Conference on Solid State Devices and Materials (SSDM2015), Sapporo, Japan, Sep. 28-30, pp.432-433 (2015) (採択率 ~70%)
- (2) Z. Lin, M. Rasly, and T. Uemura: “Electrical Detection of Nuclear Spin-Echo Signals in an Electron Spin Injection System”, 9th International School and Conference on Spintronics and Quantum Information Technology, Fukuoka, Japan, Jun. 4-8, p.177 (2017)
- (3) Z. Lin, D. Pan, M. Rasly, and T. Uemura: “Electrical spin injection into an AlGaAs/GaAsbased high-mobility two-dimensional electron system”, IEEE International Magnetism Conference 2018 (INTERMAG 2018), Singapore, Apr. 23-27, p.1616 (2018) (採択率 ~60%)
- (4) Z. Lin, D. Pan, M. Rasly, and T. Uemura: “Electrical spin injection into an AlGaAs/GaAsbased 2DEG system with a Co<sub>2</sub>MnSi spin source up to room temperature”, 2019 Joint MMM-Intermag Conference, Washington, DC, USA, Jan. 14-18 (2019) Accepted (採択率 ~60%)

## 2. 論文(その他)

- (1) M. Rasly, Z. Lin, M. Yamamoto, and T. Uemura: “Analysis of the transient response of nuclear spins in GaAs with/without nuclear magnetic resonance”, AIP Advances, Vol. 6, No. 5, 056305 (8pp) (2016) (IF=1.653, TC=2)
- (2) M. Rasly, Z. Lin, and T. Uemura: “Systematic investigations of transient response of nuclear spins in the presence of polarized electrons”, Phys. Rev. B Vol. 96, No. 18, pp. 184415 (8pp) (2017) (IF=3.813, TC=1)
- (3) M. Rasly, Z. Lin, M. Yamamoto, and T. Uemura: “Analysis of transient response of nuclear spins in GaAs with/without nuclear magnetic resonance”, 13th Joint MMM-Intermag Conference, San Diego, CA, USA, Jan. 11-15, pp.278-279 (2016) (採

採率 ~60%)

- (4) M. Rasly, Z. Lin, M. Yamamoto and T. Uemura: “Electrical control of nuclear spin polarization: Experimental and quantitative modeling”, IEEE Int’l Magnetism Conf. 2017 (INTERMAG 2017), Dublin, Ireland, Apr. 24-28, (2017) (採率 ~60%)

3. 講演 (学位論文関係)

- (1) Z. Lin, M. Yamamoto, T. Uemura, “Transient analysis of oblique Hanle signals observed in GaAs”, Extended Abstracts of the 76th Japan Society of Applied Physics Autumn Meeting 2015 (DVD-ROM), 09-117, 16p-3A-4, Nagoya Congress Center, Nagoya-shi, Sep. 13-16, 2015.
- (2) Z. Lin, M. Rasly, M. Yamamoto, and T. Uemura, “Transient analysis of oblique Hanle signals observed in GaAs based on a time evolution of nuclear spin temperature”, The 20th Symposium on the Physics and Application of Spin-Related Phenomena in Semiconductors (PASPS-20), Program and Abstracts, F-2, Tohoku Univ., Sendai-shi, December, 3–4, 2015.
- (3) Z. Lin, M. Rasly, M. Yamamoto, and T. Uemura, “Analysis of transient response of nuclear spins to a change in the magnetic field based on a time evolution of nuclear spin temperature”, The 51st Conference of Hokkaido Chapter, The Japan Society of Applied Physics, Collected Abstracts, p. 27, A-24, Sapporo-shi, January 9-10, 2016.
- (4) Z. Lin, M. Rasly, T. Uemura, “Electrical detection of nuclear spin-echo signals in an electron spin injection system”, The 64th Japan Society of Applied Physics Spring Meeting 2017, 15a-501-8, Pacifico Yokohama, Mar. 14-17, 2017.
- (5) Z. Lin, D. Pan, M. Rasly, T. Uemura, “Electrical spin injection and detection in an AlGaAs/GaAs-based high-mobility two-dimensional electron system”, The 22rd Symposium on the Physics and Application of Spin-Related Phenomena in Semiconductors (PASPS-22), Program and Abstracts, P-14, Sigma Hall, Toyonaka Campus, Osaka Univ., Osaka-shi, December, 4–5, 2017.
- (6) Z. Lin, M. Rasly, T. Uemura, “Spin-echo signals electrically detected in a spin injection device”, The 22rd Symposium on the Physics and Application of Spin-Related Phenomena in Semiconductors (PASPS-22), Program and Abstracts, O-14, Sigma Hall, Toyonaka Campus, Osaka Univ., Osaka-shi, December, 4–5, 2017.
- (7) Z. Lin, M. Rasly, T. Uemura, “Electrical spin-echo measurements in a spin injection device” (発表奨励賞), The 53rd Conference of Hokkaido Chapter, The Japan Society of Applied Physics, Collected Abstracts, p. 15, A-15, Sapporo-shi, January 6-7, 2018.
- (8) Z. Lin, D. Pan, M. Rasly, and T. Uemura, “Temperature dependence of spin signals in an AlGaAs/GaAs-based high-mobility two-dimensional electron system”, The 65th Japan Society of Applied Physics Spring Meeting 2018, 17p-D104-10, Waseda University, Nishi-Waseda Campus, Mar. 17-20, 2018.
- (9) Z. Lin, D. Pan, M. Rasly, and T. Uemura, “Electrical spin injection into an AlGaAs/GaAsbased 2DEG system with a half-metallic spin source”, The 79th Japan Society of Applied Physics Autumn Meeting 2018, 18p-PB1-30, Nagoya Congress Center, Nagoya, Sep. 18-21, 2018.